The Astrophysical Journal, 885:61 (29pp), 2019 November 1 https://doi.org/10.3847/1538-4357/ab4255

Column Density, Kinematics, and Thermal State of Metal-bearing Gas within the Virial Radius of $z \sim 2$ Star-forming Galaxies in the Keck Baryonic Structure Survey

Gwen C. Rudie[1], Charles C. Steidel[2], Max Pettini[3], Ryan F. Trainor[4], Allison L. Strom[1], Cameron B. Hummels[2], Naveen A. Reddy[5], and Alice E. Shapley[6]

[1] The Observatories of the Carnegie Institution for Science, 813 Santa Barbara Street, Pasadena, CA 91101, USA; gwen@carnegiescience.edu
[2] Cahill Center for Astronomy and Astrophysics, California Institute of Technology, MS 249-17, Pasadena, CA 91125, USA
[3] Institute of Astronomy, Madingley Road, Cambridge CB3 OHA, UK
[4] Department of Physics & Astronomy, Franklin & Marshall College, 415 Harrisburg Pike, Lancaster, PA 17603, USA
[5] Department of Physics and Astronomy, University of California, Riverside, 900 University Avenue, Riverside, CA 92521, USA
[6] Department of Physics & Astronomy, University of California, Los Angeles, 430 Portola Plaza, Los Angeles, CA 90095, USA
Received 2019 February 26; revised 2019 August 30; accepted 2019 September 5; published 2019 October 31

Abstract

We present results from the Keck Baryonic Structure Survey (KBSS) including the first detailed measurements of the column densities, kinematics, and internal energy of metal-bearing gas within the virial radius (35–100 physical kpc) of eight $\sim L^*$ galaxies at $z \sim 2$. From our full sample of 130 metal-bearing absorbers, we infer that halo gas is kinematically complex when viewed in singly, doubly, and triply ionized species. Broad O VI and C IV absorbers are detected at velocities similar to the lower-ionization gas but with a very different kinematic structure, indicating that the circumgalactic medium (CGM) is multiphase. There is a high covering fraction of metal-bearing gas within 100 kpc, including highly ionized gas such as O VI; however, observations of a single galaxy probed by a lensed background QSO suggest the size of metal-bearing clouds is small (<400 pc for all but the O VI-bearing gas). The mass in metals found within the halo is substantial, equivalent to $\gtrsim$25% of the metal mass within the interstellar medium. The gas kinematics unambiguously show that 70% of galaxies with detected metal absorption have some unbound metal-enriched gas, suggesting galactic winds may commonly eject gas from halos at $z \sim 2$. When modeled assuming that ions with different ionization potentials can originate within a single gaseous structure, significant thermal broadening is detected in CGM absorbers that dominates the internal energy of the gas. Some 40% of the detected gas has temperatures in the range $10^{4.5–5.5}$ K where cooling times are short, suggesting the CGM is dynamic, with constant heating or cooling to produce this short-lived thermal phase.

Key words: galaxies: evolution – galaxies: formation – galaxies: high-redshift – intergalactic medium – quasars: absorption lines

1. Introduction

The gaseous environments of galaxies are a crucial but poorly constrained component of galaxy formation and evolution. The circumgalactic medium (CGM) is the principal reservoir for future gas accretion, and its kinematics, thermal properties, and metal enrichment provide vital constraints on the properties of cosmological inflow and galaxy-scale outflows. Characterization of this gas therefore presents a unique window into the baryonic flows that are expected to profoundly influence the formation and evolution of galaxies.

The last decade has seen considerable growth in observations of the low-redshift CGM, in large part due to the installation of the Cosmic Origins Spectrograph on the *Hubble Space Telescope*. These observations have demonstrated that low-redshift galaxies are surrounded by substantial reservoirs of metal-enriched gas (Tumlinson et al. 2011; Liang & Chen 2014; Werk et al. 2014; Johnson et al. 2017; Zahedy et al. 2019), which correlates with the environments in which the galaxies reside (Johnson et al. 2015; Burchett et al. 2016; Nielsen et al. 2018) and the mass and star formation rate of the system (Chen et al. 2010; Tumlinson et al. 2011; Borthakur et al. 2013; Bordoloi et al. 2014; Johnson et al. 2017; Rubin et al. 2018). At low redshift, there is evidence that strong metal absorbers are more commonly found along the major and minor axes of disk galaxies (Kacprzak et al. 2012), suggestive of metal-bearing gas accreting along the major axis of the disk while metal-enriched outflows escape along the minor axis.

While our understanding of the low-z CGM is growing, arguably the best epoch in which to study the effect of gas flows on galaxy formation is $2 < z < 3$, during the peak of cosmic star formation (Madau et al. 1996) and supermassive black hole growth (Richards et al. 2006). At these redshifts, spectroscopic observations of star-forming galaxies commonly exhibit signatures of strong baryonic outflows (Pettini et al. 2001; Shapley et al. 2003; Rupke 2018). At the same time, the baryonic accretion rate onto galaxies is predicted to be near its maximum (e.g., Faucher-Giguère et al. 2011; van de Voort et al. 2011; Reddy et al. 2012b). Therefore, we expect the signatures of baryonic flows to be most readily observable at $2 < z < 3$. Absorption-line spectroscopy of bright background sources provides a uniquely sensitive probe of the physical properties and chemical compositions of gas in close proximity to galaxies.

In fact, the strong rest-UV transitions most useful for characterizing cosmic gas are more accessible in the distant universe than at low redshift. Thanks to cosmological expansion, these transitions fall in the observed optical, allowing observations with large-aperture ground-based telescopes equipped with high-dispersion spectrographs. For this reason, one can obtain higher resolution and higher signal-to-noise ratio CGM data for $z > 2$ galaxies than can be obtained for low-redshift galaxies.

Nevertheless, observational studies of the high-redshift CGM require significant observational investments, due to

the extreme faintness of typical galaxies in the distant universe, complicating the assembly of large samples of galaxy–QSO pairs. Thus, only a handful of studies at $z \gtrsim 2$ have been possible to date (Adelberger et al. 2003, 2005; Hennawi et al. 2006; Crighton et al. 2011; Rudie et al. 2012b; Rubin et al. 2015).

The first CGM studies at $z > 2$ were carried out by Adelberger et al. (2003) and Adelberger et al. (2005), who studied H I and C IV absorption surrounding over 1000 $z > 2$ Lyman break galaxies (LBGs).[7] These authors found strong correlations between the locations of galaxies and H I and C IV absorption and enhanced H I absorption on megaparsec scales. In this work, very strong correlations are reported between C IV absorbers and galaxies, suggesting strong C IV absorbers and LBGs must be residing in the same halos.

Simcoe et al. (2006) further analyzed a subset of these data, considering detailed multi-ion column density measurements from line fitting for 10 galaxies within 500 pkpc of the line of sight to HS 1700+6416. These authors also calculated photoionization corrections to determine the sizes and metallicities of gas within the CGM. Their results suggest that metal absorbers within the CGM of the galaxies are metal rich ($>0.1\ Z_{\odot}$) and small (<1 kpc), implying relatively high gas densities (1000 times the mean density at the redshift of the galaxies).

Steidel et al. (2010) stacked the spectra of many background galaxies surrounding ~500 foreground $z > 2$ LBGs to study the CGM at very close impact parameters (<125 pkpc). They found a high covering fraction and large equivalent width of H I and many metal species that declined as the impact parameter increased. Past ~60 pkpc, ionic metal line absorption is no longer detected in these stacks, so to probe the CGM at slightly higher impact parameters, a higher-fidelity measurement of the CGM absorption, such as that provided by background QSOs, is needed.

More recently, higher signal-to-noise ratio (S/N) QSO spectra have been combined with very large redshift surveys in the Keck Baryonic Structure Survey (KBSS; Rudie et al. 2012b). Rakic et al. (2012) presented the first 2D maps of H I absorption around high-z galaxies using KBSS data. These maps, measured using the pixel optical depth (POD) technique, showed megaparsec-scale enhancement in the H I optical depth surrounding galaxies. The kinematics of the H I exhibited clear signatures of gas infall on megaparsec scales and large peculiar velocities, plausibly due to gas outflows, on small scales (Rakic et al. 2012; Rudie et al. 2012b; Turner et al. 2014).

Rudie et al. (2012b) presented a detailed Voigt profile decomposition of all H I absorbers in the CGM of KBSS galaxies. We found very strong enhancements in the column density $N_{\rm H\,I}$ close to galaxies, finding typically $N_{\rm H\,I} \approx 10^{16.5}$ cm^{-2} within 100 kpc, three orders of magnitude higher than was typical at random places in the intergalactic medium (IGM). We also noted that $N_{\rm H\,I} \geqslant 10^{14.5}$ cm^{-2} absorbers correlate with the positions of galaxies, suggesting they may trace the CGM. The line widths of the H I absorbers within 300 kpc were found to be larger than typical of the IGM even when compared at fixed $N_{\rm H\,I}$, suggesting that gas within the CGM is either more turbulent or hotter.

[7] LBGs are typical star-forming galaxies in the distant universe, selected based on their blue UV continua or a strong break at 912 Å in their rest frame due to H I Lyman continuum absorption from the Ly alpha forest along their line of sight.

Turner et al. (2014) used POD analysis to study H I and metal line optical depth as a function of distance to KBSS galaxies, finding strong enhancements in metal line absorption within 180 pkpc and ±240 km s^{-1}. Turner et al. (2015) focused on gas close to the galaxies (<180 pkpc), studying the enhancement of metal line absorption, finding enhanced O VI optical depth at fixed H I, C IV, and Si IV optical depths extending to ±350 km s^{-1}. Turner et al. (2015) suggested that the O VI detected at high H I optical depth could be formed via photoionization; however, the large O VI enhancement at low H I optical depth was more consistent with collisionally ionized hot gas with relatively high metallicity ($>0.1\ Z_{\odot}$), properties most likely found within galactic winds.

In this paper we continue our analysis of the KBSS data set. Here we describe the first detailed measurements of metal line absorption within the halos of eight $z \sim 2$ galaxies, including the column densities, kinematics, and thermal state of gas within the high-z CGM. Section 2 presents the observational data including more information concerning the galaxy sample. Section 3 discusses the Voigt profile modeling of the QSO absorption-line data. In Section 4, we present our measurements of the column densities and covering fractions of metal ions in the KBSS. Section 5 covers the kinematics of metal-enriched gas, with Section 6 presenting our measurements of the temperature and turbulence within the CGM. In Section 7, we calculate the implied metal mass in the halo and compare our observations to theoretical models and other observations, discussing implications for our understanding of the CGM. A detailed summary of our results is presented in Section 8.

Throughout this paper, we assume a ΛCDM cosmology with $H_0 = 70$ km s^{-1} Mpc^{-1}, $\Omega_{\rm m} = 0.3$, and $\Omega_{\Lambda} = 0.7$. All distances are expressed in physical (proper) units unless stated otherwise. We use the abbreviations pkpc and pMpc to indicate physical units of kiloparsecs and megaparsecs.

2. Observations

The data presented here are part of the KBSS (Rudie et al. 2012b; Steidel et al. 2014; Strom et al. 2017), which combines high-resolution spectroscopy of 15 hyperluminous $2.5 < z < 2.9$ QSOs (Trainor & Steidel 2012) with large rest-optical and rest-UV galaxy redshift surveys focusing on those galaxies in the foreground of the QSO. The background QSO spectroscopy provides high-fidelity absorption-line constraints on the gas in proximity to the foreground galaxies.

The QSO data were taken with the High Resolution Echelle Spectrometer (HIRES; Vogt et al. 1994) on the Keck I telescope. All publicly available echelle spectroscopy of the QSOs was also incorporated, including both HIRES data from the Keck Observatory Archive and UVES (Dekker et al. 2000) data from the European Southern Observatory's Science Archive Facility. A detailed description of the QSO data and their reduction is provided in Rudie et al. (2012b). The final combined QSO spectra have $R \simeq 45{,}000$ (FWHM ≃ 7 km s^{-1}), S/N ~ 50–250 per pixel, covering at least the wavelength range 3100–6000 Å with no spectral gaps. The reduced QSO data were continuum normalized using low-order spline interpolation prior to the analysis of the detected absorption lines.

Foreground galaxies in the KBSS fields were selected based on their rest-frame UV colors using criteria described in Steidel et al. (2003), Adelberger et al. (2004), and Steidel et al. (2004). Optical and near-infrared (NIR) galaxy spectroscopy was

Table 1
Absorption within the Halo of KBSS Galaxies

Galaxy	z_{gal}	D_{tran} (pkpc)	$\log(\Sigma N_x)$ [cm^{-2}][a]						
			Si II	C II	Si III	C III	Si IV	C IV	O VI
Q0105-BX90b	2.3563	34.5	<12.48	<12.42	11.70	13.57	11.88	13.51	⋯
Q1442-MD50a	2.4667	56.5	12.45	13.34	12.99	⋯	13.21	14.19	13.95
Q1549-D15	2.6923	56.6	<12.58	<12.26	12.98	14.46	13.15	14.04	⋯
Q1442-MD50b	2.4360	61.9	13.95	14.69	>13.56	>14.22	14.19	>14.63	15.00
Q0142-BX182	2.3555	75.2	13.73	14.56	>13.57	>14.08	13.93	14.60	14.90
Q2343-BX551	2.1120	86.9	<12.44	⋯	13.27	⋯	13.27	14.15	⋯
Q0100-BX210	2.2769	89.6	<12.45	⋯	12.86	14.26	12.56	14.27	⋯
Q1623-BX432	2.1825	97.3	<12.37	<12.60	⋯	⋯	<12.29	<12.44	⋯

Note.
[a] Total log column density within 1000 km s^{-1}.

carried out using the Low Resolution Imaging Spectrometer (LRIS-B; Oke et al. 1995; Steidel et al. 2004) and the Multi-Object Spectrometer for Infrared Exploration (MOSFIRE; McLean et al. 2010, 2012), both on the Keck I telescope. A detailed discussion of the LRIS survey can be found in Steidel et al. (2010) and Rudie et al. (2012b). The MOSFIRE survey is discussed in Steidel et al. (2014) and Strom et al. (2017).

All of the galaxies presented herein have redshifts measured using rest-frame optical spectroscopy with Keck/MOSFIRE. These redshifts are derived from bright nebular emission lines (typically Hα and [O III]λ5007) and have associated errors $\lesssim$10 km s^{-1} (Steidel et al. 2014). Impact parameters between the QSO line of sight and the galaxy are calculated using the measured angular separation of the QSO and galaxy and the galaxy redshifts determined from the rest-optical spectra.[8] For this calculation, we assume that the galaxy redshifts are purely cosmological.

In this work, we present an analysis of gas within 100 pkpc, or roughly the virial radius (Trainor & Steidel 2012; Rakic et al. 2013; Turner et al. 2017), of galaxies in the KBSS sample. All of the galaxies included in this analysis have QSO spectroscopy covering at least two Lyman series transitions so that the H I column is well constrained. While not critical for the analysis presented herein, the well-constrained H I column densities will allow for measurements of gas-phase metallicities in future work. The names of the galaxies, their redshifts, and the impact parameter to the line of sight to the QSO are listed in Table 1. The KBSS galaxy sample probed within R_{vir} comprises eight galaxies and is the first published sample of high-redshift CGM constraints on these scales. The absorption within the KBSS high-z halos is complex, providing a statistical sample of 130 metal-bearing absorbers. Future work will present metal line analysis at larger distances for the full KBSS sample.

The $2.1 < z < 2.7$ galaxies considered in this paper (aside from Q0105-BX90b, see below) have stellar masses $9 < \log(M_*/M_\odot) < 10.7$ and star formation rates of $7 < \mathrm{SFR} < 52\ M_\odot\ \mathrm{yr}^{-1}$ determined through spectral energy distribution fits to their broadband photometry (Strom et al. 2017). The galaxies are drawn from a representative sample of typical star-forming galaxies at $z \sim 2$ characterized by the following properties. The parent sample of galaxies are young (~50 Myr–1 Gyr, Erb et al. 2006; Reddy et al. 2012a; Theios et al. 2019) and gas rich (Erb et al. 2006; Tacconi et al. 2010), with gas-phase oxygen abundances $12 + \log(\mathrm{O/H}) = 8.37$, $Z = 0.5Z_\odot$ (Strom et al. 2018). Due to their young ages and high star formation rates, they exhibit comparatively Fe-poor stellar populations that have a 1–4 Ryd ionizing spectrum that is harder than is typical in the local universe, but likely common at high redshift (Steidel et al. 2014, 2016; Strom et al. 2017). Clustering analysis of the parent sample suggests these galaxies occupy dark matter halos with median halo masses $M_{halo} = 10^{11.9}\ M_\odot$ (Trainor & Steidel 2012; Rakic et al. 2013; Turner et al. 2017), corresponding to a typical virial radius of ~100 pkpc at these redshifts.

The closest galaxy in the sample, Q0105-BX90b, was serendipitously found during MOSFIRE spectroscopic observations of another UV-color selected galaxy. BX90b lies only 4″ from the QSO line of sight, where the wings of the point-spread function from the bright QSO make accurate photometry of faint sources difficult. Due to this and the faintness of the galaxy, its full properties are hard to quantify accurately with the photometry we have in hand. We estimate that BX90b is at least 1 mag fainter than typical KBSS galaxies ($\mathcal{R} \sim 26$; $K_s \sim 25$), which would also place it at or below the low-mass end of the KBSS stellar mass distribution, that is, $M_* < 10^9\ M_\odot$.

3. Analysis of the QSO Absorption Spectra

In this section, we describe the fitting methodology used to measure the redshifts, column densities, and line widths of metal absorbers within 100 pkpc of galaxies in the KBSS survey. We model absorbers in the QSO spectra using a series of Voigt profiles, allowing us to constrain the bulk and internal kinematics of the gaseous structures.

Section 3.1 explains how thermal and nonthermal broadening can be measured using this data. Section 3.2 describes observational evidence for two phases of absorbing gas, one that appears in all species with ionization potentials <48 eV, and a separate O VI-bearing phase. We model these two phases separately as described in Sections 3.3 and 3.4, respectively.

3.1. Thermal and Turbulent Broadening of Absorbers

In this work, we present the first measurements of the temperature and turbulent velocities of gas in the high-z CGM.

[8] One of the QSOs in our sample (Q0142) is lensed (see Section 7.2), so we calculate the distance between the galaxy and the location of the brightest image at the redshift of the galaxy. The two images are only separated 400 pc from each other at the redshift of the galaxy.

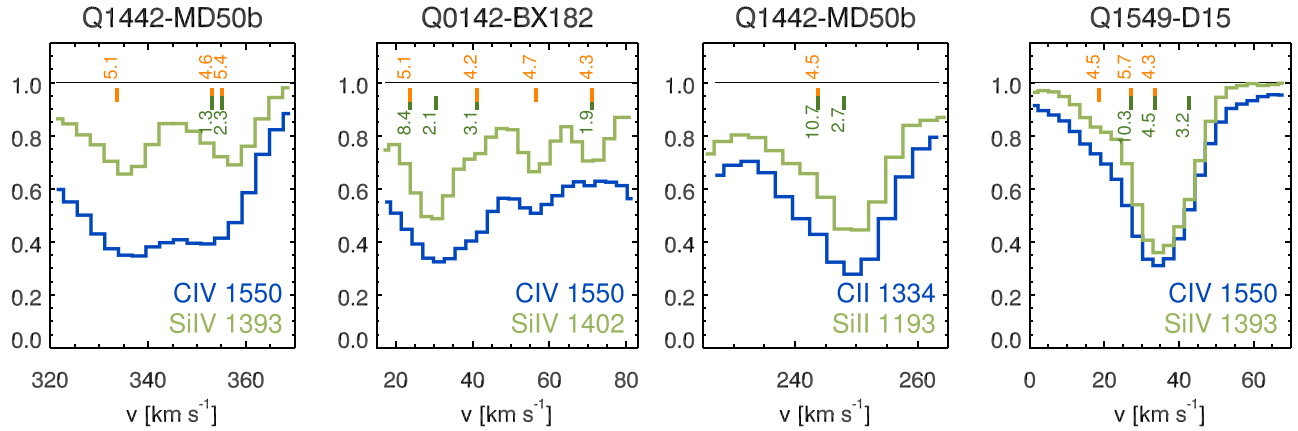

Figure 1. Examples of thermally (left two panels) and turbulently (right two panels) broadened absorption systems within the CGM of KBSS galaxies. The blue and green curves are the continuum-normalized QSO spectrum plotted with respect to the systemic redshift of the galaxy. Each panel shows one transition of C (dark blue) and one transition of Si (light green). Because these elements have different atomic masses, the widths of their respective absorption lines can be used to differentiate between thermal and turbulent broadening. Note that each panel compares either triply ionized species or singly ionized species such that ionization differences between the elements are minimized. The two left panels show absorbers where the internal energy of the absorber is dominated by thermal energy. In this case, the widths of the silicon absorption lines are appreciably narrower than those of carbon. The two right-hand panels show cases where the absorbers are dominated by turbulent broadening, in which case the widths of the absorption lines from different-mass elements are the same. Tick marks show the location of individual components of the Voigt profile fits to these data. Orange ticks show the locations of thermally broadened lines with inferred temperatures $T > 10^4$ K, which are labeled with the log of the temperature in Kelvin inferred from the fit. Green ticks are turbulently broadened absorbers with measures $v_{\rm turb} > 1$ km s^{-1} and are labeled with the turbulent velocity inferred from the fit in km s^{-1}. Note that some absorbers are found to have little to no detected thermal or turbulent broadening (those with only one tick), while most absorbers are measured to have some level of both thermal and turbulent broadening (those with both thermal and turbulent ticks).

These measurements are enabled by the very high S/N and high resolution of our data ($R \simeq 45{,}000$, FWHM $\simeq 7$ km s^{-1}), which resolve the internal broadening of absorber subcomponents. For single ionization stages, one measures the absorption line width, parameterized in Voigt profiles as the Doppler width, $b_{\rm d} = \sqrt{2}\,\sigma$, where σ is the one-dimensional velocity dispersion of the gas (along the line of sight), which depends on the combined effect of all motions of the atoms or ions in the gas cloud. There are several possible physical scenarios that lead to the broadening of IGM and CGM absorbers. Most relevant to this work are the effects of gas temperature and bulk motions of the gas (hereafter referred to as turbulence).[9]

For an isothermal gas cloud, the observed thermal broadening depends on the temperature of the gas, T, and the mass of the ion, m:

$$b_{\rm therm}^2 = \frac{2kT}{m} \tag{1}$$

where $b_{\rm therm}$ is the thermal component of the Doppler parameter and k is the Boltzmann constant. For nonthermal broadening such as turbulence, the velocity within the gas is the same for all species and does not depend on the masses of the ions.

When transitions from multiple elements are observed arising from the same gaseous structure, it is possible to decompose the broadening of each absorber into thermal and nonthermal components. For example, in the case of absorbers detected in C IV and Si IV,

$$b_{\rm C\,IV}^2 = b_{\rm turb}^2 + b_{\rm C\,IV,\,therm}^2 = v_{\rm turb}^2 + \frac{2kT}{m_{\rm C}} \tag{2}$$

$$b_{\rm Si\,IV}^2 = b_{\rm turb}^2 + b_{\rm Si\,IV,\,therm}^2 = v_{\rm turb}^2 + \frac{2kT}{m_{\rm Si}}, \tag{3}$$

where $v_{\rm turb}$ is the turbulent velocity. Because the atomic masses of Si and C differ by a factor of 2.3, with measurements of $b_{\rm C\,IV}$ and $b_{\rm Si\,IV}$ it is possible to solve for T and $v_{\rm turb}$.

In practice, for typical gas temperatures in the IGM of 2×10^4 K (Hui & Gnedin 1997; Schaye et al. 1999; Rudie et al. 2012a), the thermal broadening for C absorbers is $\sim$5 km s^{-1} and for Si absorbers is $\sim$3 km s^{-1}, which are at the resolution limit of our data; however, for higher gas temperatures and turbulent velocities, which appear to be common in the CGM at $z \sim 2$, the broadening can be more easily detected. Figure 1 shows examples of several absorption complexes in the CGM of KBSS galaxies. The left two panels show clear evidence of thermal broadening: the heavier ion (Si, shown in light green) has narrower line widths than the lighter element (C, shown in dark blue). The right two panels show CGM absorbers where the silicon and carbon profiles appear quite similar, which requires that thermal broadening be subdominant.

As we describe below, we use the joint constraint provided by multiple elements (typically carbon and silicon) to constrain the thermal and turbulent energy of the gas. While in principle absorbers detected in one metal ion as well as H I can also be used to constrain T and $v_{\rm turb}$ (see Tripp et al. 2008; Kim et al. 2016), in the $z \sim 2.3$ CGM, most H I absorbers have multiple metal absorption components detected within their velocity range, making their association ambiguous (the thermal broadening of H I in 2×10^4 K gas is $b_{\rm H\,I,therm} = 18$ km s^{-1}). For this reason, we do not compare the Doppler widths of H I with those of metal transitions to constrain the gas temperature or turbulence.

Note that the measurement of gas temperature and turbulence from these data is only possible if individual kinematic components (those fit with a single Voigt profile) can be resolved in the data. Further, the measurement requires that

[9] Another plausible source of broadening for the most physically extended absorbers with sizes >50–100 kpc is differential Hubble flow across gas "clouds" (see Rudie et al. 2012a). This source of broadening is likely only common in low-$N_{\rm H\,I}$ absorbers.

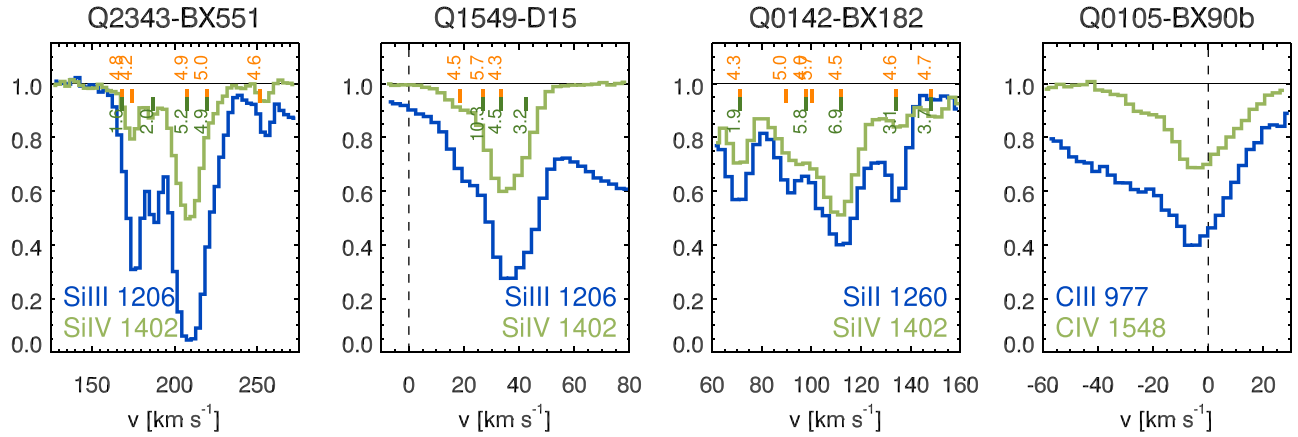

Figure 2. Examples of the kinematic similarity of absorption-line profiles of ions of the same element with different ionization potentials. The blue and green curves are the continuum-normalized QSO spectrum plotted with respect to the systemic redshift of the galaxy. Each panel shows two ions of either C or Si, with the lower ionization level plotted in dark blue and the higher ionization level plotted in light green. As each panel shows ionization states of a single element, differences in line width would be attributed to difference in the thermal or nonthermal motions of gas with different ionization states. Notably, even though the ionization potentials of these transitions are quite different, the overall kinematic structure of the components detected in both species are very similar, suggesting that the gas within the CGM harbors a variety of ionization states within the same gaseous structure and that the assumptions outlined in Section 3.1 should generally hold for these absorbers.

the gas within a single detectable absorption component resulting from species with different ionization potentials traces the same underlying gas, which is roughly isothermal and shares the same nonthermal motions. The next section demonstrates that the absorption-line data for halo gas surrounding KBSS galaxies support this physical scenario.

We caution that while the quantities T and $v_{\rm turb}$ are separable in the way described above, uncertainties in the Doppler widths propagate into the thermal and turbulent broadening measurements, causing the two quantities to be correlated. The detection of additional elements, particularly more massive elements (such as iron), would improve our ability to disentangle the two quantities. However, in practice, Fe absorption is rarely detected in the CGM of these galaxies. Section 3.3 describes in detail how we measure T and $v_{\rm turb}$ in this sample, and Section 6 discusses the results of these measurements.

3.2. Observational Evidence That the CGM Is Multiphase

Visual inspection of the data suggests that low-, intermediate-, and high-ionization species with ionization potentials less than 48 eV (equal to or lower than that of C IV) typically share the same subcomponent structure where detected (see Figures 2 and 3). Figure 2 compares the absorber line shapes of like-element ions with different ionization potentials. The lack of variation in the line widths of these absorbers with significantly different ionization potentials supports the physical scenario in which single gaseous structures contain gas of a variety of ionization states, and in which the various ionization states do not appear to be highly stratified with significantly different kinematics.

Further, while the kinematic structure in the gas is often complex (see Figure 3), the similarity of all of these components suggests that the low, intermediate, and high ions (excluding N V and O VI, see Section 3.4) are cospatial within the CGM. For these reasons, each detected subcomponent (absorption modeled with a single Voigt profile) is presumed to exist in all of the ionization stages of the various metal species with ionization potentials less than 48 eV (i.e., C II, C III, C IV, Si II, Si III, Si IV) and is presumed to share a common internal gas temperature and turbulence.

Conversely, O VI (and the rarely detected N V) does not appear to have the same kinematic structure as the lower-ionization gas. When the path length corresponding to O VI absorption is free of contamination, the observed O VI is found at the same velocities as the lower-ionization gas, but the O VI is distributed in a small number of broad absorption systems, suggestive of a very different origin than the lower-ionization gas (as has been previously reported in the high-z IGM; Simcoe et al. 2002.)

Given the very different spectral morphology of the O VI-bearing gas from that seen in lower-ionization potential species, the data support the view of the CGM as multiphase. In this scenario, the gas giving rise to O VI absorption has potentially very different densities and temperatures than the lower-ionization gas.

As such, O VI and N V are not assumed to have the same component structure as the lower-ionization species. These broad features, which are also often detected in C IV (see Figure 3), are modeled with multiple ionic transitions as well; however, the choice of which ions are included is motivated by both the data and by collisional and photoionization nonequilibrium models (Oppenheimer & Schaye 2013; Gnat 2017), as described in Section 3.4.

3.3. Voigt Profile Fitting

In order to model the absorption signal due to gas in the halos of the KBSS galaxies, we decompose the absorption into a series of Voigt profiles. Each absorber complex contains a variable number of subcomponents. Each component is modeled with a single redshift and a single value for the gas temperature and turbulent broadening of the absorber, but with column densities that vary for each unique ionization state of each element. In practice, most commonly, we detect some subset of C II, C III, C IV, Si II, Si III, Si IV, and O VI, with other ions detected less frequently. In the case where the measured temperature of the gas in an individual subcomponent is too hot to expect low-ionization stages to exist (see Section 3.4), we model that subcomponent with high-ionization species only.

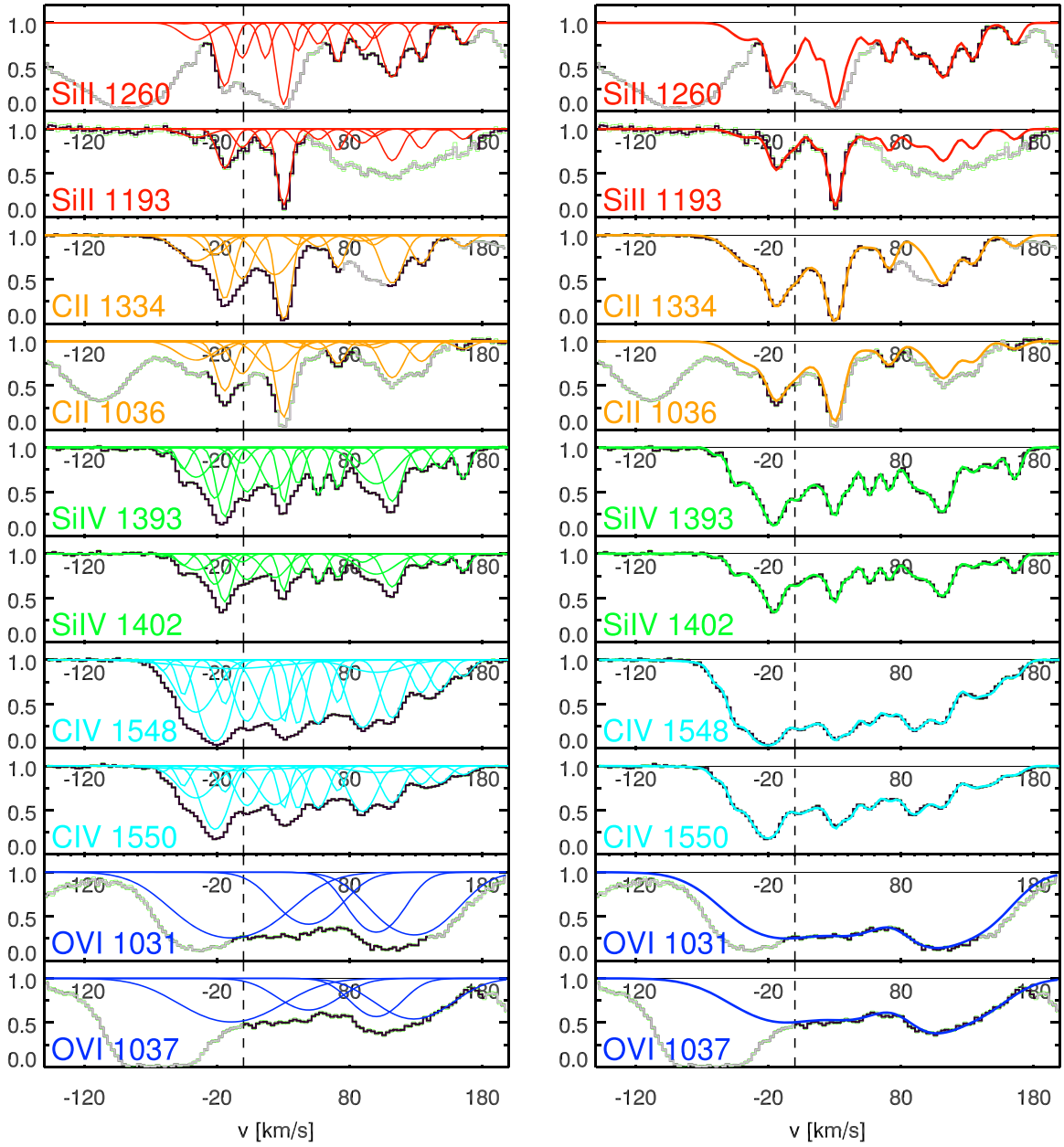

Figure 3. Example of the complex multicomponent absorption structure within the halo of Q0142-BX182, one of the most complex systems in the KBSS sample. The velocity scale is given with respect to the systemic redshift of the galaxy, measured based on strong rest-frame optical emission lines (Hα, [O III]). The continuum-normalized QSO spectrum is shown in black. The green curves that trace the black QSO spectrum with little to no deviation indicate the $\pm 1\sigma$ error on the normalized flux. Gray sections of the QSO spectrum are highlighted to show regions where there is contamination from H I or other metal ions within the wavelength range fit. Colored curves show the Voigt profile decomposition of the absorption. The left-hand panel shows the individual component structure, while the right-hand panel shows their product, which can be used to compare directly to the data to test the goodness of fit. Note that strong absorption is detected in multiple ionization phases. C III and Si III absorption is also detected (not shown) but is saturated and so is not useful for comparing the subcomponent structure. Note that the same pattern of absorption features is present in the low- and high-ion gas, but not in O VI. Some of the broad features seen in O VI do appear in the fit to C IV. We suggest that the gas observed in Si II–C IV represents a single phase, while the broad features detected in O VI and C IV represent a second phase. Plots of the absorption spectra of metal lines within the halo of other KBSS galaxies are shown in the Appendix.

In order to measure the parameters of absorbers in the CGM of KBSS galaxies, we employ VPFIT[10] written by R. F. Carswell and J. K. Webb. VPFIT is a χ^2 minimization Voigt profile fitting program designed to fit complex blends of multiple absorption components in order to derive the physical parameters of the gas. The output of VPFIT includes the measured column densities (N), Doppler widths ($b_{\rm d}$), and redshifts of absorbers, as well as errors on all of the above parameters. It is also possible to tie the constraints on the Doppler widths of multiple elements in the same component in order to constrain T and $v_{\rm turb}$ directly. In order to derive meaningful fits to the complex absorption systems associated with galaxies, detailed initial estimates of the component structure and parameters of each absorber are required.

The process of locating metal line absorption in the KBSS QSO spectra is significantly aided by the high signal-to-noise ratio of our QSO data. Typical KBSS QSO spectra have

[10] In this work, we run version 9.5 of VPFIT. VPFIT is available at https://www.ast.cam.ac.uk/~rfc/vpfit.html.

S/N ~ 100 in the regions redward of the Ly alpha forest, where many metal lines are detected. Due to the high S/N of the data, deviations in the continuum are nearly always true absorption systems, so a visual inspection of the QSO spectra in the regions of interest can identify the locations of metal absorption systems. However, given the complexity of some of the metal systems, we prefer to automate the initial fitting of absorbers.

For the initial fit, we typically use the C IV section of the spectrum to make estimates of the location and component structure of the absorbers. We employ C IV absorbers because their spectral range is mostly free of contamination and because C IV absorption is strong in these systems.[11] An automated search using custom-built code is conducted within regions of the spectrum corresponding to C IV absorption within ± 1400 km s^{-1} of the systemic redshift of galaxies.[12] Absorbers are located through cross-correlation of a representative template absorber (a single nonsaturated Gaussian absorber) with the HIRES spectrum. Peaks in the cross-correlation are presumed to be the locations of individual absorption components, which are subsequently fit with a Gaussian to estimate their widths and column densities. This method is analogous to that used to make initial estimates for H I absorbers in the spectra as described in Rudie et al. (2012b).

Once initial estimates of the parameters of C IV absorbers are complete, the parameters are input into VPFIT. The output of VPFIT is checked by eye, and the number of components and their parameters are adjusted and iteratively rerun until an appropriate fit to the C IV absorbers is achieved (reduced $\chi^2 \approx 1$).

Once an appropriate fit to C IV is complete, the parameters of the C IV fit are duplicated for Si IV but with column densities $N_{\rm Si\,IV}$ adjusted to match the optical depth of the detected Si IV components. The redshifts of the various subcomponents in C IV and Si IV are tied, and the parameters of the initial guesses are again passed to VPFIT. VPFIT then solves for the tied redshift of each component as well as the column densities ($N_{\rm C\,IV}$ and $N_{\rm Si\,IV}$) and Doppler widths ($b_{\rm C\,IV}$ and $b_{\rm Si\,IV}$), which are allowed to vary independently. Solutions with matching subcomponent structures in both ions are preferred; however, in some cases absorption is detected in one ion only. For such absorbers, the undetected component is dropped from the fit to the ion in which it is not detected.

Absorbers fit jointly in Si IV and C IV typically have Doppler widths with $b_{\rm C\,IV} \gtrsim b_{\rm Si\,IV}$, as expected in the case of thermal broadening because C is lighter than Si. As Si IV absorbers are often found to be narrower than their C IV counterparts, occasionally, unrecognized subcomponents are identified in the Si IV data, in which case the component is added to both the Si IV and C IV fits and VPFIT is rerun.

Once a satisfactory fit is achieved for Si IV and C IV, their Doppler widths are used to determine the temperature (T) and turbulent velocity ($v_{\rm turb}$) of each component using Equations (2) and (3). The Doppler widths of the two transitions are then tied with a single value of the temperature (T) and turbulent velocity ($v_{\rm turb}$) for each component, and VPFIT is rerun providing measurements and uncertainties for the physical parameters (T and $v_{\rm turb}$) rather than the model parameters ($b_{\rm C\,IV}$ and $b_{\rm Si\,IV}$).

Using the output of this round of fitting, duplicate components are added in lower-ionization stages where detected (typically some subset of C II, C III, Si II, and Si III), now with tied redshifts, T, and $v_{\rm turb}$.[13] The column densities of the newly added ions are again scaled to roughly match the observed optical depths in those species, and the full set of estimates are again run through VPFIT. As with the combined Si IV and C IV, occasionally components need to be added in order to produce a satisfactory fit to the lower-ionization data, and undetected components in individual ions are dropped from the fit to that ion.

In one instance (Q0100-BX210, which has a particularly complex subcomponent structure), VPFIT would not converge when allowed to fit for T and $v_{\rm turb}$; however, in this system, the determined $b_{\rm C\,IV}/b_{\rm Si\,IV} \approx \sqrt{m_{\rm Si}/m_{\rm C}}$, the ratio expected in the case of pure thermal broadening, so the fit for that system was run assuming $b_{\rm C\,IV}/b_{\rm Si\,IV} = \sqrt{m_{\rm Si}/m_{\rm C}}$. This represents 8/130 of the absorbers reported in this work. Similarly, in seven absorbers with weakly detected and highly blended metal lines, the determined $b_{\rm C\,IV}$ and $b_{\rm Si\,IV}$ were roughly equal and were fixed to purely turbulent broadening to improve the convergence of VPFIT.

We favor Voigt profile fits that have the minimum number of subcomponents required to produce an adequate fit. However, given the complex nature of some of the absorption systems seen in the CGM, unrecognized blended components are possible. Given that a large fraction of the absorbers with multielement constraints are consistent with nearly pure thermal broadening (see Section 6), we expect that the effect of unrecognized blends is minimal.

The final result of the fitting process is a list of the detected column densities of the various ionic transitions for each subcomponent as well as their redshift, gas temperature T, and turbulent velocity $v_{\rm turb}$. In cases where a subcomponent is detected for only one element, T and $v_{\rm turb}$ are not constrained, and only N, z, and $b_{\rm d}$ are measured.

3.4. O VI

The final step of the Voigt profile decomposition deals with O VI, the species with the highest ionization potential detected in these data. O VI is a challenging ion to constrain in the high-z CGM because the wavelength of the O VI doublet $\lambda\lambda$1031,1037 Å is very similar to the wavelength of the Lyman β transition (λ 1025), which is ubiquitous in the high-z IGM. Thus, in many cases, our data are too contaminated by high-column-density H I systems to measure O VI; however, the doublet is detectable and quite strong in others. As shown in Figure 3, the spectral morphology of O VI, where detected, is very different from that seen in the ions with lower ionization potential. In particular, while the lower ions show many narrow subcomponents, the O VI section of the spectrum typically exhibits a handful of very broad absorbers that are less apparent in the lower ions.

However, in the systems with the strongest detected O VI components, the C IV fit described in the previous section (which has no constraint provided by the O VI portion of the spectrum) typically contains several broad components that are

[11] For one galaxy in the sample, Q0142-BX182, the absorption component structure is sufficiently blended in C IV that we opt instead to use the Si IV section of the spectrum.

[12] We use ± 1400 km s^{-1} as a conservative upper limit on the velocity based on the results of H I studies of the CGM of KBSS galaxies (Rudie et al. 2012b).

[13] Note that all ionization states detected in a given component are fit assuming the same value of T and $v_{\rm turb}$.

well matched with those seen in O VI but with significantly lower optical depths (see Figure 3). Given that the O VI region of the spectrum is not included as a constraint in the C IV fit up to this point, the data in the C IV region independently prefer the presence of broad components.

Given that the broad C IV components typically overlap in redshift space with the narrower components, their fits are often uncertain. In order to better constrain the properties of these broad absorbers, we introduce the O VI section of the spectrum to the fit and tie the redshifts and Doppler parameters of broad O VI components to broad lower-ionization lines where detected and rerun VPFIT.

There are no visually apparent broad components in ions with ionization potentials below that of Si IV. Further, the expectation (given their very different ionization potentials) would be that O VI-bearing gas would not contain singly ionized species. However, given the fitting procedure defined above, in some cases the fit to low-ionization species such as C II and Si II also includes broad components, while in others these components have been dropped by VPFIT.

For initially hot gas radiatively cooling to $T \lesssim 10^6$ K, nonequilibrium ionization effects are likely due to the short cooling times at these temperatures. Rapid radiative cooling leads to the recombination of the gas lagging behind the drop in temperature, resulting in overionization of the gas compared to collisional ionization equilibrium (CIE) predictions (see, e.g., Gnat & Sternberg 2007; Oppenheimer & Schaye 2013). Oppenheimer & Schaye (2013) and Gnat (2017) revisited this non-CIE calculation while including the presence of radiation. We use these nonequilibrium cooling models to determine the expected ionic phases for broad components consistent with high gas temperatures. In the following, we consider all absorbers with temperature determinations, regardless of the detection or lack thereof of O VI.

Based on these comparisons to the models from Gnat (2017), we remove all of the low-ionization fit components with inferred temperatures $\log(T/\mathrm{K}) \gg 5$. For absorption components with $\log(T/\mathrm{K}) \approx 5$ and those with $\log(T/\mathrm{K}) \gg 5$ detected in the doubly ionized phase or Si IV, we consider the column density ratios of various ions and their errors as well as the error on the temperature measurements. In cases where the inferred ion ratios and temperatures are implausible for all model tracks, we again remove that component of the fit to the lower-ionization species in question. In total, 11/130 kinematically distinct absorbers are altered in this procedure, all with inferred $\log(T/\mathrm{K}) > 5$. Broken down by ionization state, we remove six Si II components, five C II components, two Si III components, three C III components, and one Si IV component from the fits to these 11 absorbers. Once components with unphysical parameters are removed, we rerun VPFIT. The output of this final run forms the basis for the conclusions in this paper.

4. Column Densities and Covering Fractions

The gas within the CGM of high-z galaxies is kinematically complex and multiphase (see Figure 3). We commonly detect gas from singly ionized through triply ionized species at the same velocities and with overall similar profiles. Higher-ionization gas, such as that exhibiting O VI absorption, is less kinematically complex and bears little resemblance to the lower-ionization gas, implying a very different origin.

Table 2
Component Structure of Absorption Line Fits

Galaxy	#[a]							
	all	Si II	C II	Si III	C III	Si IV	C IV	O VI
Q0105-BX90b	12	0	0	2	9	7[b]	12	⋯
Q1442-MD50a	15	4	8	5	⋯	10	14	3
Q1549-D15	15	0	0	10	9	9	13	⋯
Q1442-MD50b	31	20	18	⋯[c]	⋯[c]	18	19	12
Q0142-BX182	25	15	15	⋯[c]	⋯[c]	20	20	4
Q2343-BX551	8	0	⋯	7	⋯	6	7	⋯
Q0100-BX210	24	0	⋯	9	14	10	22	⋯
Q1623-BX432	0	0	0	⋯	⋯	0	0	⋯
Mean[d]	19	13	14	7	11	11	15	6
Median[d]	15	15	15	7	9	10	14	4
Max	31	20	18	10	14	20	22	12

Notes.
[a] The number of metal-line Voigt profile components in the fit. The first column gives the number of unique kinematic components fit considering all ions. The subsequent columns give the number of components included in the fit to each species.
[b] Most of the Si IV absorbers included in this fit are not significantly detected, but they are not dropped by VPFIT. We do not use these components to derive temperatures in Section 6, but these components are included in the covering fraction and total column density calculations.
[c] Because these ions are highly saturated, their component structure is not well determined, so we do not report a value.
[d] The median and mean refer to the median and mean number of components per galaxy among those galaxies in which the ion was detected. Note that for each ionization state, the sample of galaxies in which gas is detected is different (see Table 1).

The Voigt profile decompositions of metal line detections in the sample vary in their complexity. Individual galaxies in the sample contain anywhere from zero to 31 metal line components with a median (mean) of 15 (19) components per galaxy (Table 2). Broken down by ionization state, galaxies with detected absorption in a given ion typically have >10 components within $\pm$1000 km s^{-1} (Table 2).

4.1. Column Densities

To quantitatively assess the frequency of detection of multiple species and the quantity of gas found in each ionization state, here we present statistics based on both the maximum column density absorber in each ion, $\max(N_x)$, and the total column density in each ion, ΣN_x (Table 1). The column densities range from nondetections to $\log(\Sigma N_x) > 14.6$. For one galaxy (Q1623-BX432), we detect no metal absorption down to relatively sensitive limits ($\log(N_x) \lesssim 12.5$, see Figure 4 and Table 1). While this is the galaxy with the largest impact parameter presented here, we note that strong metal line absorption is detected within the more extended halos of many galaxies at larger impact parameters within the KBSS (G. C. Rudie et al., in preparation).

Figure 4 shows the statistics for $\max(N_x)$ and ΣN_x as a function of impact parameter. KBSS galaxies have large quantities of ionized metals in their CGM, with a typical $N_{\mathrm{C\,IV}} > 10^{14}$ cm^{-2}. Singly ionized species are more commonly detected closer to galaxies. We do not detect singly ionized C or Si beyond 75 pkpc in this sample. However, all galaxies

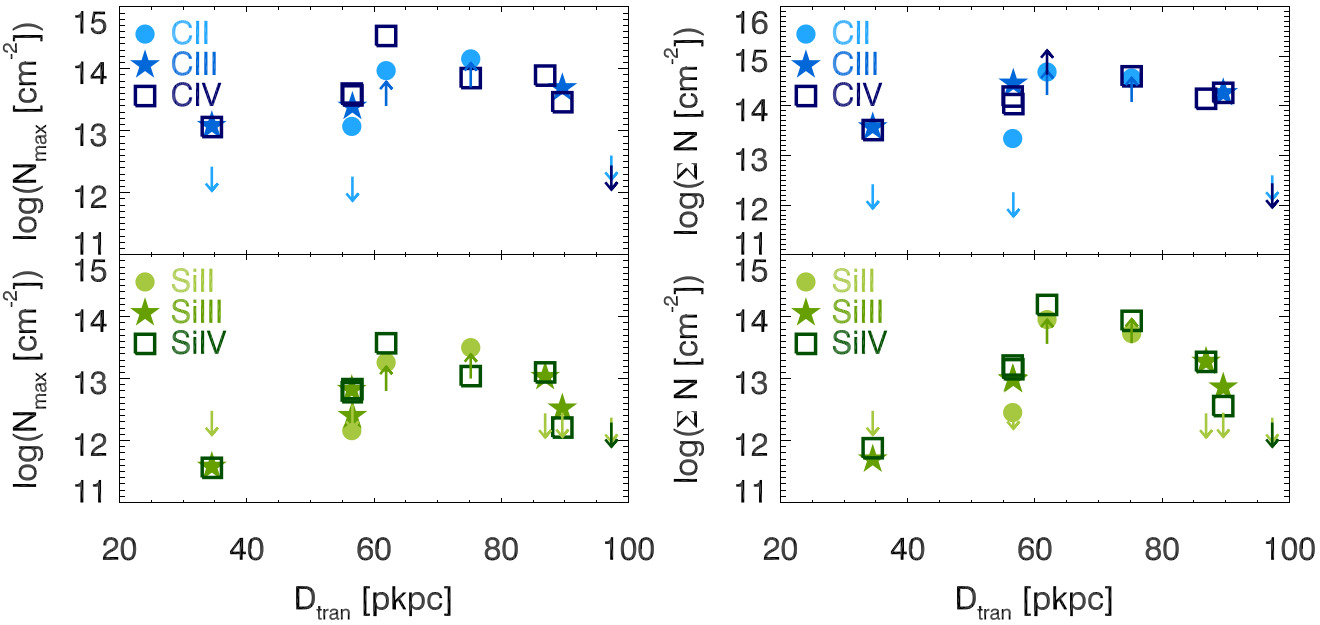

Figure 4. The highest column density absorber, max(N_x) (left panel), and the total column density, ΣN_x (right panel), in each of six species as a function of impact parameter between the galaxy and the line of sight to the QSO. Downward-pointing arrows correspond to nondetections, while upward-pointing arrows represent saturated absorbers with lower limits on the column density. Note that due to the similar impact parameters of Q1442-MD50a and Q1549-D15, the column densities corresponding to those galaxies appear overplotted. The closest galaxy in the sample, Q0105-BX90b, is likely lower in mass than the rest of the KBSS galaxies (see text for details), so its relatively low column densities may not be typical of the population. All galaxies within 90 pkpc have absorption in one or more ionization state of C and Si. Halo gas at $z \sim 2$ contains large column densities of metal ions.

within 90 pkpc have detected absorption in one or more ionization state of C and Si.

With $D_{\rm tran} = 35$ pkpc, Q0105-BX90b has the smallest impact parameter in the current sample; however, as discussed in Section 2, it also has a significantly lower stellar mass than the other sample galaxies. Therefore, the low measured column densities of metallic ions at small galactocentric distance are probably not representative of more typical KBSS galaxies. However, even if Q0105-BX90b is removed, the maximum and total column densities are not monotonic or strongly correlated with impact parameter within $R_{\rm vir}$. This is unsurprising given the small sample size and small dynamic range in impact parameter presented here. Future work will present measurements of C IV and Si IV at larger distances, which do show the expected strong anticorrelation between impact parameter and column density, although with considerable scatter (G. C. Rudie et al., in preparation).

For well-detected and nonsaturated absorbers, max(N_x) and ΣN_x are well defined. However, in the case of saturation or nondetections, we place lower or upper limits, respectively, on max(N_x) and ΣN_x, as described in the next section.

4.2. Nondetections and Saturated Systems

For ions in which all observed transitions are saturated (or for singlets that are saturated), we estimate a lower limit on the total column density in the saturated velocity range by computing the equivalent width in the saturated regions and converting it to a column density using the linear portion of the curve of growth. This lower limit on the column density is treated as a single absorber and added to the catalog. To compute ΣN_x, we add the determined N_x to that of all of the unsaturated components, and we report the total column density as a limit.

For ions where some or all of the transitions are uncontaminated, but where the ions are still not detected, we compute upper limits on the column density. These limits are derived by computing the limiting equivalent width within the velocity range surrounding each galaxy in which the transmission in the Lyα regions drops below 80%. For highly contaminated regions, we do not report a column density limit.

4.3. Covering Fractions

With column density measurements and limits in hand, we can also calculate the covering fraction of halo gas as a function of ionization state and limiting column density. Figures 5 and 6 show the measured covering fraction of gas of various ionization states within 100 kpc of galaxies in the KBSS.

The covering fraction of gas is defined as the number of galaxies with detected absorption above a limiting column density divided by the number of galaxies in which it would be possible to detect absorption above that limit. In Figures 5 and 6 the value of the number of galaxies with detections and the number of galaxies where the measurement is possible is printed above the bar in each bin of column density and ion.

To measure the covering fraction, we use the upper limits derived for nondetections in Section 4.2 to determine if the absorption-line data for a given galaxy are sufficient to detect absorbers of a given N_x. Galaxies without detections that (1) have spectral coverage of the ion in question, (2) are not strongly contaminated, and (3) have sufficiently sensitive spectra contribute to the denominator of the covering fraction for a given limiting column density (the $x$axis in Figures 5 and 6). For this reason, as the value of the limiting N_x declines, the number of galaxies with sufficiently sensitive spectra decreases as well, and so the value of the denominator declines.

Note that for some ionization states, there are galaxies without spectral coverage of some transition (C III). Similarly,

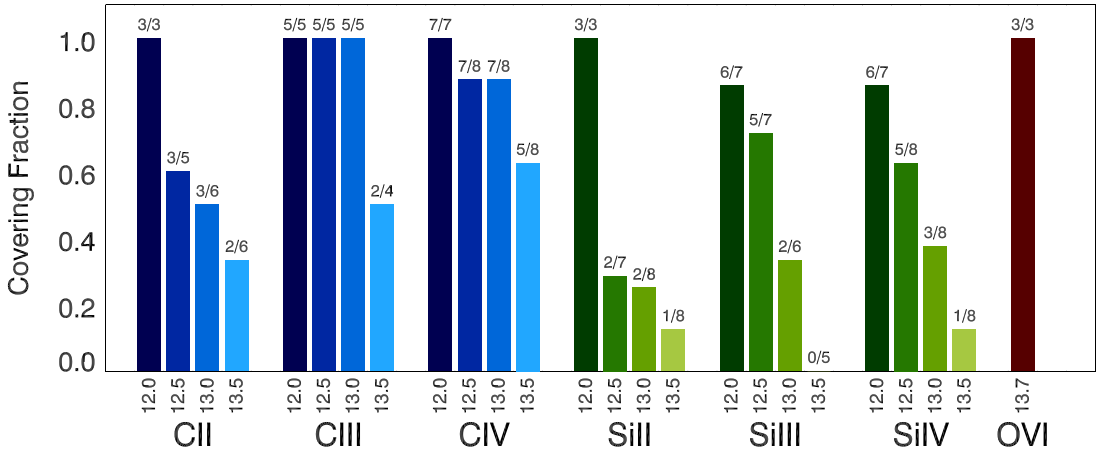

Figure 5. Covering fractions of various ionic species within 100 pkpc and ±1000 km s^{-1} of galaxies in the KBSS. These values are determined using the column densities of individual components in the Voigt profile decomposition. Note that in systems with the most sensitive data, all of the ionization states of carbon are always detected. For higher column densities [$\log(N_x/\mathrm{cm}^{-2}) = 12$–12.5], at which all of the uncontaminated sight lines in the sample are sensitive, the covering fraction for all three ionization stages of carbon is >50%. Si III and Si IV show equally high covering fraction; only Si II is detected less frequently than 50% within the halo of these galaxies.

for some galaxies, the absorption-line spectra of particular ions (C II, C III, Si III, O VI) are too heavily contaminated to be useful probes of the covering fraction. These galaxies do not contribute to the measurement of the covering fraction for any ions in which their absorption-line spectra are insensitive.

Figure 5 shows the covering fraction as a function of the column densities of individual absorbers, while Figure 6 considers the same statistic for ΣN_x within ±1000 km s^{-1}. Note that at low column densities [$\log(N_x/\mathrm{cm}^{-2}) = 12$–12.5], the covering fraction for doubly and triply ionized species is very high, 87%–100%. At higher column densities, the covering fractions decline; however, the covering fraction of C IV remains >50% even for $N_{\mathrm{C\,IV}} \geqslant 10^{13.5}$ cm^{-2}.

4.4. O VI

Because O VI is located within the Lyβ forest, it suffers significantly more contamination than other ions discussed in this work. In velocity ranges where H I and C IV absorption is detected and where the O VI portion of the spectrum is not highly contaminated (three galaxies), there are clear detections of O VI with relatively high $N_{\mathrm{O\,VI}} \sim 10^{14}$ cm^{-2}. In velocity ranges with greater contamination, all of the sight lines are consistent with having O VI absorption with $N_{\mathrm{O\,VI}} > 10^{14}$ cm^{-2}; however, in such cases, the component structure of O VI absorption, if present, is not sufficiently constrained for fitting. The data are therefore consistent with a 100% covering fraction for $N_{\mathrm{O\,VI}} \geqslant 10^{13.7}$ cm^{-2} and $\Sigma N_{\mathrm{O\,VI}} \geqslant 10^{13.9}$ cm^{-2}, as shown in Figures 5 and 6.

While the data are often sufficiently contaminated that it is challenging to make unambiguous measurements of the O VI column, there are reasons to suspect that there is O VI absorption and that the column densities may typically be large ($N_{\mathrm{O\,VI}} \sim 10^{14}$ cm^{-2}). First, we compute limits on the O VI column density by measuring the equivalent width of possible O VI in the velocity regions with high H I opacity within ±1400 km s^{-1} of the systemic velocity of the galaxies. In 7/8 of the galaxies, the velocity regions containing the highest inferred O VI equivalent widths were the velocity regions closest to the systemic redshift of the galaxy. If all of the absorption in the O VI regions were due to contamination, one would expect more scatter in the velocity range of the highest apparent opacity.

Other circumstantial evidence of O VI absorption comes from a comparison of the O VI section of the spectrum with that of C IV. If one assumes O VI is coincident in velocity space with C IV absorption, as is the case for regions where O VI is detected with high confidence, the data are typically consistent with $N_{\mathrm{O\,VI}}/N_{\mathrm{C\,IV}} \geqslant 1$.

Additional support for the common existence of a substantial O VI-bearing phase comes from a POD analysis of the KBSS sample. Turner et al. (2015) found strongly enhanced O VI absorption at fixed H I, C IV, and Si IV optical depths within 180 pkpc and ±350 km s^{-1} of KBSS galaxies compared to random locations in the spectra. The strength of the detected O VI absorption and the high O VI-to-H I optical depth ratios found imply that the most plausible excitation mechanism for some of the O VI-bearing gas is collisional ionization in a $T > 10^5$ K gas with metallicity of at least 10% solar. Given the high inferred metallicity, velocities in excess of the circular velocity of the halo, and that these conditions were found uniquely in regions close to galaxies, Turner et al. (2015) conclude the most likely source would be galactic wind material. The O VI absorption shown in Figure 3 and clearly detected in the other uncontaminated systems is consistent with this interpretation.

4.5. Comparison to Theory and Other Observations

Recently, Peeples et al. (2019) created mock spectra of sight lines passing through a zoom-in simulation of a Milky Way–like halo at $z > 2$ in the FOGGIE simulation. FOGGIE is one of several recent simulations employing enhanced halo resolution (forced refinement within the CGM, Hummels et al. 2019), allowing them to resolve the detailed structure of halo gas (Hummels et al. 2019; Peeples et al. 2019; Suresh et al. 2019; van de Voort et al. 2019). Peeples et al. (2019) do not report the general statistics for the number of components found along randomly drawn sight lines, instead focusing on the number found along simulated sight lines containing high-column-density H I absorbers ($N_{\mathrm{H\,I}} > 10^{17}$ cm^{-2}; Lyman limit systems, LLS). In these simulations, the median number of C IV (Si IV) components found along LLS-bearing sight lines is three (five), significantly lower than our median number of components of 14 (10; see Table 2). This comparison suggests

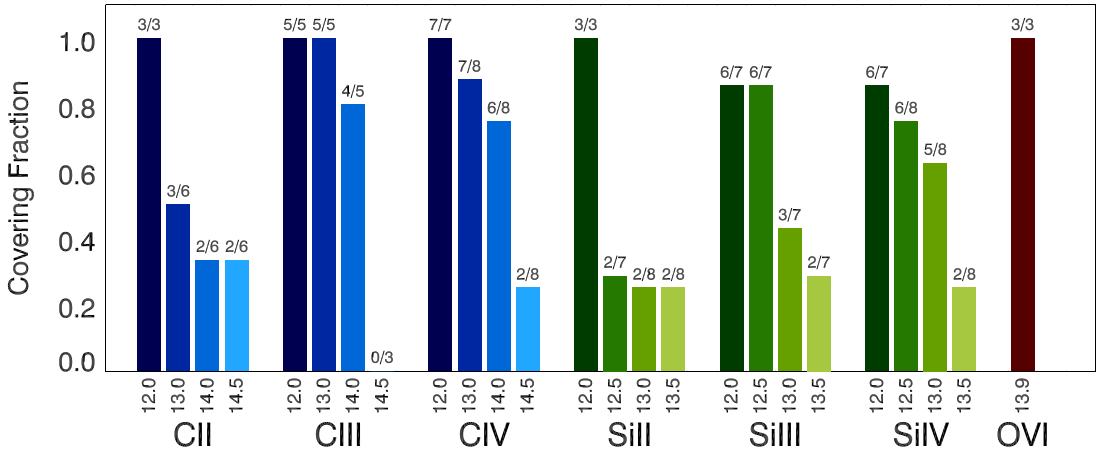

Figure 6. Same as Figure 5 (the covering fraction of various species within 100 pkpc), but calculated for the total column density within ±1000 km s^{-1}, $\Sigma N_{\rm ion}$.

there may be CGM structures that remain unresolved even in simulations such as FOGGIE (Hummels et al. 2019); however, given the mismatch in the selection of lines of sight in FOGGIE and the sample presented here, a more direct comparison should be made before stronger conclusions can be drawn.

Shen et al. (2013) computed the covering fraction of various ions surrounding the Eris2 simulated galaxy. Eris2 is matched to the Milky Way mass at $z = 0$ and so is certainly less massive than the majority of the KBSS galaxies. Shen et al. (2013) report the covering fractions for $N_x > 10^{13}$ cm^{-2} for each ion within $R_{\rm vir}$. Compared with our observations (Figure 6), they find a consistent covering fraction of Si IV ($C_f \sim 70\%$), C IV ($C_f \sim 90\%$), and O VI ($C_f = 100\%$), but their simulations overproduce the covering fraction of C II ($C_f \sim 70\%$) and Si II ($C_f \sim 40\%$) compared to the KBSS observations ($C_{f,\rm C\,II} = 50\%$ and $C_{f,\rm Si\,II} = 30\%$) within $R_{\rm vir}$.

Liang et al. (2016) analyzed simulations that evolved into a Milky Way mass galaxy at $z = 0$ (lower mass than is typical of the KBSS at $z \sim 2.3$), considering the radial profile of H I and metals surrounding galaxies as a function of redshift. For the snapshots at $z = 2$ and $z = 3$ compared at radial distances scaled by the virial radius of the halo, the typical column densities seen in the simulations underpredict that seen in the KBSS data for H I and C IV. For H I, Rudie et al. (2012b) report a typical $N_{\rm H\,I} = 10^{16.5}$ cm^{-2} within $0.5 < R/R_{\rm vir} < 1.0$, whereas the simulations of Liang et al. (2016) have typical $N_{\rm H\,I} < 10^{14}$ cm^{-2} at $z = 2$ and $10^{14} < N_{\rm H\,I} < 10^{15}$ cm^{-2} at $z = 3$. For C IV, over one-half of the KBSS sight lines within $R_{\rm vir}$ have $N_{\rm C\,IV} > 10^{14.0}$ cm^{-2}, while Liang et al. (2016) find $N_{\rm C\,IV} < 10^{12.0}$ cm^{-2} at $z = 2$ and $N_{\rm C\,IV} < 10^{13.0}$ cm^{-2} at $z = 3$ for all of their simulations except for one. At $z = 3$, the C IV column densities predicted for a model with more energetic supernovae are somewhat higher ($10^{12} < N_{\rm C\,IV} < 10^{14.5}$ cm^{-2}), closer to the observed value. Similarly, the O VI column densities are somewhat lower than observed in all models ($10^{13} < N_{\rm O\,VI} < 10^{14}$ cm^{-2} at $z = 2$ and $z = 3$, whereas KBSS galaxies have $N_{\rm O\,VI} > 10^{13.9}$ cm^{-2}), with the closest model being the $z = 3$ snapshot with more energetic supernovae ($10^{13.5} < N_{\rm O\,VI} < 10^{14}$ cm^{-2}).

Again we note that the mass scales of the Liang et al. (2016) and Shen et al. (2013) simulations were meant to match a Milky Way progenitor and are therefore less massive than is typical of the KBSS galaxies. This limits the utility of detailed comparisons with these models. Simulations with galaxy properties more similar to the KBSS would be more useful in diagnosing any discrepancies between the data and current models, which could lead to a better understanding of the nature of accretion and feedback in the distant universe.

The measured O VI column densities ($N_{\rm O\,VI} > 10^{13.9}$ cm^{-2}) are similar to the typical O VI columns found surrounding low-redshift galaxies (Werk et al. 2013; Johnson et al. 2015, 2017; Zahedy et al. 2019) and also the typical column densities of low-redshift O VI systems found in random sight-line surveys (Thom & Chen 2008; Chen & Mulchaey 2009; Savage et al. 2014). Several theoretical models have successfully reproduced these high column densities, using a variety of physical scenarios and assumptions (Heckman et al. 2002; Shen et al. 2013; Bordoloi et al. 2017; Faerman et al. 2017; McQuinn & Werk 2018; Oppenheimer et al. 2018; Qu & Bregman 2018; Stern et al. 2018; Voit 2019), suggesting the column densities alone may not be sufficient to discriminate between models and that more detailed observations that further constrain the nature of O VI absorbers are needed. In Section 6, we discuss constraints on the widths of O VI absorbers, and temperatures where possible, in a first attempt to provide these more detailed constraints.

5. Gas Kinematics

The kinematics of gas in the CGM of high-z galaxies offers important clues about the baryon cycle. One quantity of particular importance is the fractions of mass and metals that are ejected from the ISM of the galaxy through galactic winds, many of which reside within the CGM. Additionally, understanding the fate of galactic winds once outside the ISM is critical; the chemical evolution of galaxies is strongly coupled to the amount of metals lost from the system via galactic winds versus the amount that may return to the galaxy as "recycled" material (see, e.g., Shapiro & Field 1976; Oppenheimer et al. 2010; Anglés-Alcázar et al. 2017).

Assessing the fate of metal-enriched material is complicated by our limited knowledge of the 3D kinematics of gas with respect to galaxies. In particular, in CGM studies, we can only observe the redshift of absorbers from which we derive constraints on both the radial velocity of the gas and its position along the line of sight. Due to the ambiguity between position and velocity, it is not generally possible to determine the *direction* of motion of an individual absorber into or out of the galaxy. Past work has instead relied on ensemble statistics and comparisons to analytic scalings such as the circular velocity (e.g., Rakic et al. 2012; Rudie et al. 2012b.)

Given that we can only measure the *line-of-sight velocity* of the gas, the measured difference in redshift between the galaxy

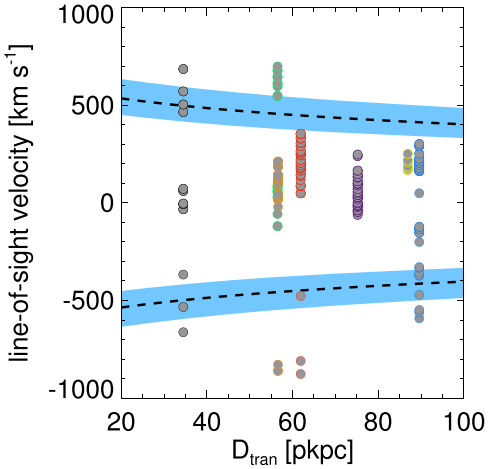

Figure 7. Velocities and impact parameters of metal-enriched absorbers within 100 pkpc of a galaxy in the KBSS sample. Errors in velocity and impact parameter are smaller than the symbol size. Each distinct galaxy is plotted with a different-color outer annulus so that the points corresponding to Q1442-MD50a and Q1549-D15 can be differentiated. Plotted for comparison is the 3D escape velocity as a function of distance for halos of $\log(M_{\rm halo}/M_{\odot}) = 11.9$ (black dashed line) and $11.7 < \log(M_{\rm halo}/M_{\odot}) < 12.1$ (blue shading). Notably, for 5/7 galaxies, we detect metal-enriched absorbers at velocities well in excess of the escape velocity, implying that some of the detected CGM is unbound to the galaxies.

and the absorber, Δv, provides only a lower limit on the true 3D velocity of the gas. The only unambiguous interpretation is for measured line-of-sight velocities larger than the escape velocity at a given projected distance ($\Delta v > v_{\rm esc}$). In such systems, we can say with certainty that the gas is not bound to the galaxy, although it is still not possible to know with certainty that the gas originated within the galaxy in question.

Figure 7 shows the measured velocities of absorbers with respect to the systemic velocity of their closest known galaxy, and how the velocities relate to the impact parameter between the galaxy and the absorbers. When interpreting this figure, it is important to keep in mind that the impact parameter $D_{\rm tran}$ is always a lower limit on the 3D distance between the galaxy and the absorber, and the velocity is always also a lower limit on the true 3D velocity of the gas with respect to the galaxy.

We compare the measured velocities of absorbers to the expected escape velocities of halos in the following way. We compute the escape velocity as a function of 3D distance from a Navarro–Frenk–White halo (Navarro et al. 1997) with virial masses of $11.7 < \log(M_{\rm halo}/M_{\odot}) < 12.1$. We assume a halo concentration of 3.0 following Duffy et al. (2008). The mass range is selected to be the range of halo masses that reproduces the measured clustering of KBSS galaxies (Trainor & Steidel 2012).[14] The escape velocities are plotted in Figure 7 as the blue band. The black dashed curve highlights the escape velocity for a $\log(M_{\rm halo}/M_{\odot}) = 11.9$ halo, the median halo mass of galaxies in our sample.

Notably, 5/7 (70%) of the galaxies for which we detect metals within the virial radius exhibit metal-enriched gas at velocities well in excess of the escape velocity of their halos. For points that lie outside the blue shaded regions, we can say *unambiguously* that the gas is not bound to the galaxy in question. This is in contrast to low-redshift observations, which have generally found absorbers with measured radial velocities well below the escape velocity of their halos (Tumlinson et al. 2011; Stocke et al. 2013; Zhu et al. 2014; Borthakur et al. 2016; Huang et al. 2016; Werk et al. 2016), although see Tripp et al. (2011) and Borthakur et al. (2016) for some examples of gas with $\Delta v > v_{\rm esc}$.

As with all CGM metal-bearing absorption systems, it is possible that the metals in the unbound absorbers were not ejected from the galaxies in question, but arise from some other source.[15] But given the high fraction of KBSS galaxies with detected unbound absorbers, we consider the probability of such a scenario to be low.

Further, the velocities of the unbound absorbers are not unexpected. KBSS galaxies commonly show strong signatures of outflowing ISM, detected through blueshifted UV interstellar absorption lines (Shapley et al. 2003; Steidel et al. 2010). KBSS rest-UV spectra typically show outflow velocities as high as 800 km s^{-1} in low-ionization gas as well as high-ionization species such as C IV. The location of this absorbing gas is uncertain, but it is certainly plausible that the unbound gas we detect within the halo results from the high-velocity outflows commonly seen in these galaxies.

While it is not possible to say definitively which absorbers are bound to the galaxy,[16] the nature of the unbound absorbers is of considerable interest. In Figure 8 we compare the velocity distribution of absorbers of a variety of ionization stages to understand if absorbers at high velocity are different from those closer to the systemic velocity of the galaxy. The top panel shows singly ionized species, followed by doubly ionized species, while the two lower panels show highly ionized metal species (Si IV, C IV, N V, O VI) and absorbers with $\log(N_{\rm H\,I}/{\rm cm}^{-2}) > 14.5$. Notably, the velocity distribution of highly ionized absorbers extends to higher overall velocities; however, the general velocity distribution of absorbers is similar. For low, intermediate, and highly ionized absorbers, 8 ± 4%, 17 ± 6%, and 18 ± 4% of absorbers have $|\Delta v| > v_{\rm esc}$. For absorbers with $|\Delta v| > v_{\rm esc}$, the median of $|\Delta v|$ is 650, 610, and 600 km s^{-1} but with median absolute deviations of 40, 50, and 100 km s^{-1} for low, intermediate, and highly ionized absorbers, again reflecting that the highest velocity absorbers are detected only in highly ionized species. Also notable is the comparative lack of $N_{\rm H\,I} > 10^{14.5}$ cm^{-2} absorbers that are unbound (bottom panel).

Clearly, the unbound CGM gas is multiphase, similar to other gas within the CGM. The unbound metal absorbers typically appear to be associated with lower $N_{\rm H\,I}$, suggesting they are either highly ionized, metal rich, or both.

[14] Trainor & Steidel (2012) report that halos with a minimum halo mass $M_{\rm halo,min} = 10^{11.7}\,M_{\odot}$ reproduce the clustering of the KBSS galaxies. Based on the halo mass function above $M_{\rm halo,min} = 10^{11.7}\,M_{\odot}$, the median mass is $M_{\rm halo} = 10^{11.9}\,M_{\odot}$, and we choose $11.7 < \log(M_{\rm halo}/M_{\odot}) < 12.1$ to encompass the majority of halos of galaxies in the sample. Rakic et al. (2013) used H I absorption in the CGM in comparison with hydrodynamic simulations, finding $M_{\rm halo,min} = 10^{11.6}\,M_{\odot}$, consistent with Trainor & Steidel (2012). If we instead use the stellar mass–halo mass relation at $z = 2$ from Behroozi et al. (2013) and the maximum mass of the galaxies in the sample $M_{*} = 10^{10.7}\,M_{\odot}$, we would compute a maximum halo mass of $M_{\rm halo} = 10^{12.2}\,M_{\odot}$, which would not change the results presented herein.

[15] We note that within 100 kpc, we have spectroscopic redshifts for the majority of galaxies that meet our photometric selection criteria. As such, if these high-velocity absorbers are due to other clustered galaxies, they would have to be due to lower-luminosity galaxies than those considered here.

[16] Absorbers in Figure 7 that lie between the two curves have more ambiguous kinematics. Because $D_{\rm tran}$ is a lower limit on the 3D distance and Δv is a lower limit on the 3D velocity of the absorbers, those absorbers that appear to have $|v| < v_{\rm esc}$ could truly be bound to the galaxy, or they could be more distant or moving sufficiently fast along the plane of the sky that they are actually unbound.

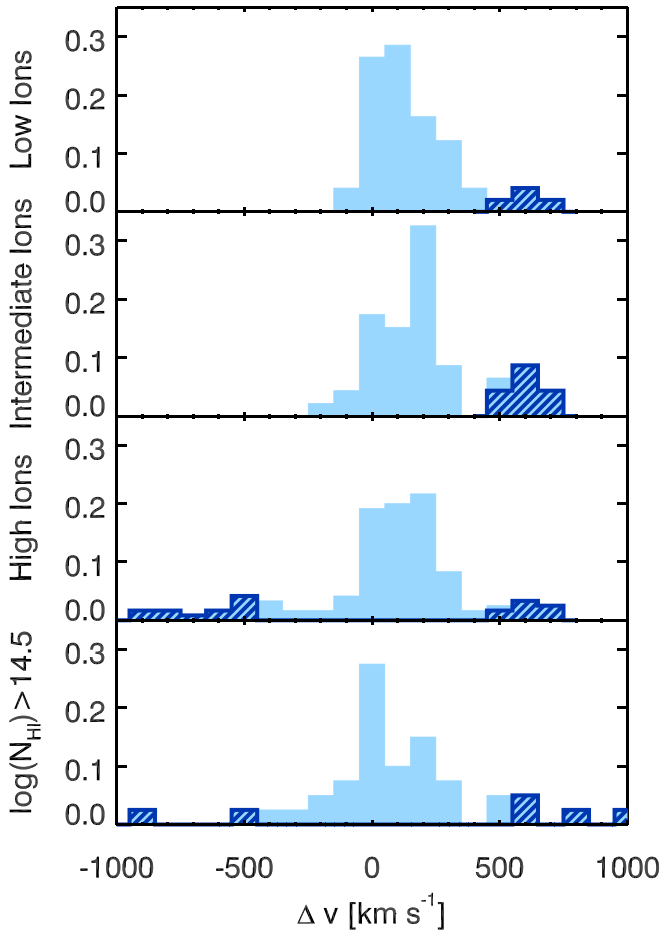

Figure 8. Normalized velocity distribution of absorbers of various ionization potentials. "Low ions" refers to absorbers with detected C II or Si II absorption, intermediate ions are C III or Si III, and high ions are C IV, Si IV, N V, or O VI. Also included for comparison are high-$N_{\rm H\,I}$ absorbers [with $\log(N_{\rm H\,I}/{\rm cm}^{-2}) > 14.5$], which were shown in Rudie et al. (2012b) to correlate strongly with the positions of galaxies. The dark blue hatched histogram represents those absorbers with $\Delta v > v_{\rm esc}$ for a dark matter halo mass $\log(M_{\rm halo}/M_{\odot}) = 11.9$, as shown in Figure 7. Note that the velocity distribution of high ions is more extended toward higher velocities, and that a higher fraction of the unbound absorbers are detected in high ions. Most of the unbound absorbers do not show strong H I absorption, as can be seen in the bottom panel. The bias toward redshifted systems relative to the galaxies' systemic velocities is likely due to the small number of galaxies (seven) contributing to this measurement.

The largest number of unbound absorbers is detected in C IV absorption. Among the five galaxies with detected unbound C IV, $\gtrsim$20% of the C IV column density is unbound. Considering all of the detected C IV, $\gtrsim$12% of the halo C IV column density is unbound.

Given the large velocity offset of the unbound absorbers as well as their high level of ionization or enrichment, the most plausible source of these absorbers is galactic winds, likely the same source as the O VI absorption discussed in Turner et al. (2015) and Section 4.4. These data demonstrate that some of this gas, if it belongs to a galactic wind, has traveled large fractions of $R_{\rm vir}$ and still has sufficient velocity to escape the halo. The calculation above suggests a substantial fraction of the highly ionized halo gas may be unbound.

6. Temperature and Turbulence of Gas in the $z \sim 2$ CGM

As described in Section 3, in addition to providing kinematic information for gas within the CGM, the KBSS data also constrain the temperature and internal turbulence of gas within the halos of these galaxies. Within the last decade, much of the theoretical literature concerning the CGM has focused on the temperature and structure of accreting gas. The theoretical consensus is that most galaxies at early times do not form stable shocks at or near the virial radius of their dark matter halo because most have yet to build a massive, virialized hot halo. And even after stable shocks have formed, for some dense filamentary gas configurations, much of the gas may still accrete without drastic heating (Birnboim & Dekel 2003; Kereš et al. 2005; Ocvirk et al. 2008; Brooks et al. 2009; Benson & Bower 2011; van de Voort et al. 2011). In these models, the filamentary structure of the cosmic web can penetrate the halos of even relatively massive ($M_{\rm halo} \approx 10^{12}\ M_{\odot}$) galaxies, allowing efficient accretion of diffuse intergalactic material into the ISM of these early galaxies. The KBSS galaxies, with $M_{\rm halo} = 10^{12}\ M_{\odot}$, provide a compelling test of this theoretical consensus.

In Rudie et al. (2012b), we studied the Doppler width ($b_{\rm d}$) distribution of H I absorbers in the CGM of KBSS galaxies, finding that $b_{\rm d,\ H\,I}$ compared at fixed $N_{\rm H\,I}$ were higher close to galaxies than at random places in the IGM. These results suggested that gas within the CGM was either more turbulent or hotter. However, without the constraint provided by metal ions, we could not determine whether their broadening was due to higher gas temperatures or larger gas turbulence.

The analysis presented herein includes a total of 130 detected metal-bearing absorbers, all within 100 pkpc impact parameter (roughly $R_{\rm vir}$) of a galaxy in the KBSS. With the additional analysis of metal absorption, we can address the source of line broadening within the gas. As discussed in Section 3, differentiating between thermal and turbulent broadening of absorption systems requires the detection of at least two ions from elements with significantly different atomic masses (such as Si and C). Of the 130 absorbers, 93 (72%) are detected in multiple metal ions covering at least two elements, making it possible to constrain their thermal and turbulent broadening. For all other absorbers, it is possible to place only upper limits on their gas temperature by assuming pure thermal broadening. Figure 9 shows the distribution of inferred gas temperatures for the full sample with multielement measurements in the top panel and single-element absorbers with upper limits of the gas temperature shown in the bottom panel.[17] For completeness, we also show the measurements with $T > 2\sigma_T$ in light blue in the upper panel. The three sets have median inferred temperatures of $\log(T/{\rm K})$ of 4.37, 4.67, and 5.00 for all of the detections, the high-S/N sample, and the limits, respectively. The median temperature for the entire sample (including upper limits) is $\log(T/{\rm K}) = 4.5$.

This temperature distribution is notable for several reasons. First, the gas spans >2 orders of magnitude in temperature, even when only considering the highest-significance measurements. Second, 40% of the absorbers with measured gas temperatures (as well as 40% of absorbers with upper limits) have inferred gas temperature between $4.5 < \log(T/{\rm K}) < 5.5$, with an additional 6% (10% including limits) with $\log(T/{\rm K}) > 5.5$.

[17] We note that all of the metal absorbers presented have associated hydrogen absorption; however, there are typically many metallic components whose associated hydrogen is completely blended. Thus, for the complex absorbers that seem to be characteristic of the CGM of L^* galaxies at $z \sim 2$, it is not possible to use the relative widths of H I and some metallic transition to determine the gas temperature and turbulence.

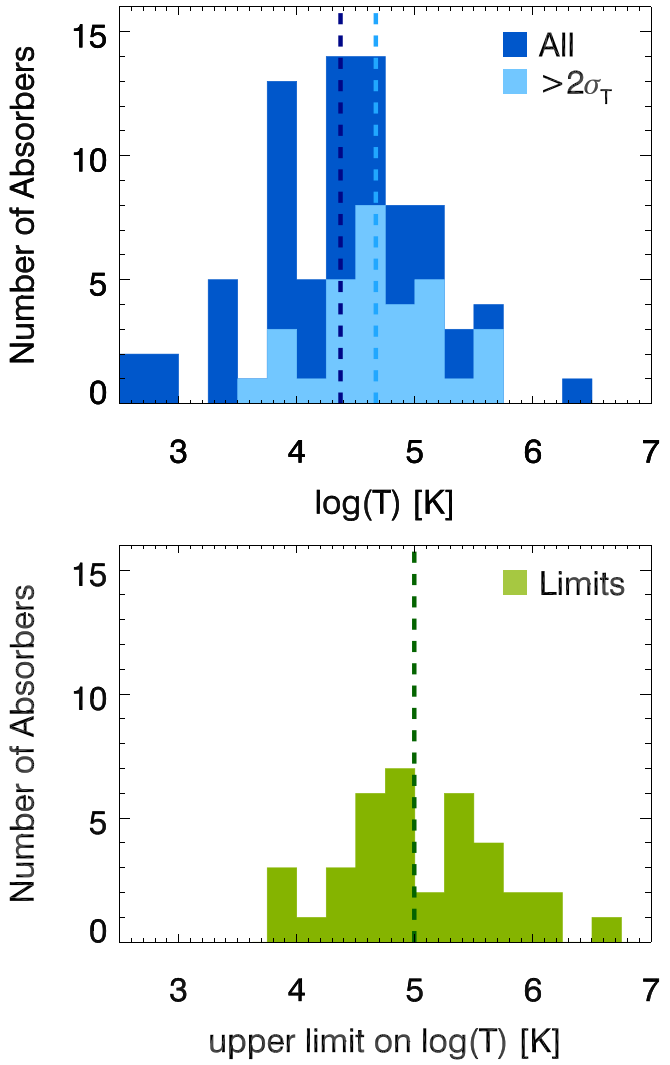

Figure 9. Distribution of inferred gas temperatures and upper limits for the full sample of absorbers excluding those fit with pure turbulent broadening (see Section 3). The upper panel shows the distribution of inferred gas temperature for the 80 absorbers with detected thermal broadening and inferred temperatures $T > 10^{2.5}$ K. The darker shaded histogram shows all of the measurements, while the lighter shaded histogram show absorbers with $>2\sigma$ measurements of T. The median temperature for all of the multielement measurements is $\log(T/\mathrm{K}) = 4.37$, shown in the dark blue vertical dashed line, while for the high-S/N sample, the median is $\log(T/\mathrm{K}) = 4.67$, shown in the light blue line. The lower panel shows the upper limits on the gas temperature for absorbers detected in only one element. The median value of these limits, shown by the vertical green line, is $\log(T/\mathrm{K}) = 5.00$.

In addition to constraining the gas temperature, the sample with multielement detections can also be used to measure the internal velocity dispersion of individual gaseous structures, henceforth referred to as turbulence.[18] Note that we do not measure the turbulence of the ensemble of "clouds" within the virial radius of a galaxy halo, but rather the dispersion of gas within a separable gaseous structure fit with a single Voigt profile.

Figure 10 shows the measured turbulent velocities. Most of the studied gas in the inner CGM has relatively low measured

[18] This measurement also presumes that ions of different ionization stages that appear to result from a single CGM structure all trace gas with the same underlying internal gas motions.

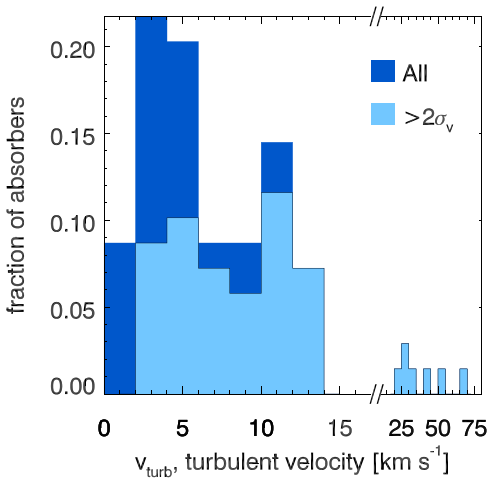

Figure 10. Same as the top panel of Figure 9 but showing the turbulent velocity distribution of absorbers with detected turbulent broadening. The median turbulent velocity is $v_{\rm turb} = 5.8$ km s^{-1} with an interquartile range of $3.7 < v_{\rm turb} < 10.7$ km s^{-1}; 90% have $v_{\rm turb} < 15$ km s^{-1}.

turbulence. The median turbulent velocity is $v_{\rm turb} = 5.8$ km s^{-1} with an interquartile range of $3.7 < v_{\rm turb} < 10.7$ km s^{-1}; 90% have $v_{\rm turb} < 15$ km s^{-1}.

6.1. Internal Energy of Halo Gas

To compare the measured thermal and turbulent properties of the CGM, we compare the thermal and turbulent components of the internal energy of the gas. The energy per particle from the kinetic temperature of the gas is

$$E_T = \frac{1}{\gamma - 1} kT = \frac{3}{2} kT, \tag{4}$$

where $\gamma = 5/3$ for a monatomic gas. This can be compared to the energy per particle due to the internal turbulence within the gaseous structures:

$$E_{\rm turb} = \frac{1}{2} \mu m_p v^2, \tag{5}$$

where $\mu = 0.6$ is the assumed mean molecular weight, $m_{\rm p}$ is the proton mass, and k is the Boltzmann constant.

Figure 11 compares the thermal energy to the total internal energy in the gas. Notably, 58% of absorbers fit with a thermal +turbulent model have >90% of their energy coming from thermal contributions, while only 18% have more turbulent than thermal energy. Clearly most of the internal energy in the gas comes from its temperature rather than bulk motions.

These data also provide a measurement of the sonic nature of turbulence within the circumgalactic gas. For each absorber where the thermal and nonthermal broadening is measured, one can infer the sound speed of the gas as well as its turbulent velocity. The sound speed is given by

$$c_s^2 = \frac{\gamma kT}{\mu m_p}. \tag{6}$$

Substituting the sound speed into Equation (4) in place of the gas temperature results in the following relationship:

$$\frac{E_T}{E_{\rm Total}} = \frac{1}{1 + \frac{\gamma(\gamma-1)}{2}\frac{v^2}{c_s^2}} = \frac{1}{1 + \frac{5}{9}\mathcal{M}^2}, \tag{7}$$

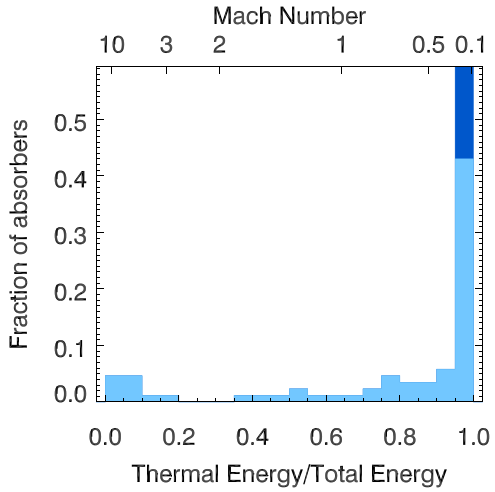

Figure 11. Fraction of the total internal kinetic energy attributed to thermal energy compared to the total kinetic energy from both nonthermal and thermal energy. The light blue histogram shows that a large fraction of the absorbers have much more thermal energy than kinetic energy from turbulence. The additional absorbers shown in dark blue are those fit with a pure thermal model. Notably, 58% of absorbers fit with a thermal+turbulent model have >90% of their energy coming from thermal contributions, while only 18% have more turbulent than thermal energy. The top axis shows the implied Mach number of the internal gas turbulence; 80% of absorbers have subsonic internal turbulence.

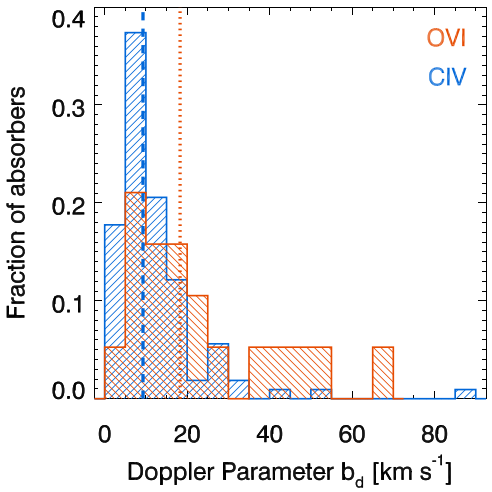

Figure 12. Measured Doppler width of O VI-bearing absorption components (red) compared to C IV-bearing absorption components (blue). The median Doppler parameters of the samples are shown in the blue dashed (O VI) and red dotted (O VI) lines. Clearly, the typical O VI absorber has significantly more thermal or nonthermal broadening than the typical C IV absorber. However, there exist a population of broad C IV absorption systems.

where $\mathcal{M} = v/c_s$ is the Mach number of the gas motion internal to each absorber.[19]

Figure 11 shows the results of this calculation on the top *x*axis. Clearly, the turbulent velocity *within* the majority of absorbers is subsonic, with 80% of absorbers with measured thermal and turbulent broadening having $\mathcal{M} < 1.0$. However, while the internal velocities within absorbers appear to typically be subsonic, it is clear from Figure 7 that many of the absorbers with $v > v_{\rm esc}$ are likely to have bulk motions that are supersonic if their 3D location is in fact within the halos in question.

Note that the measurements of gas temperature in the top panel of Figure 9 and the turbulent velocity measurements in Figure 10 require that ions of different ionization stages are present in the same gaseous structures and that their respective widths trace the same underlying temperature and turbulence of the gas. As discussed in Section 3.2 and shown in Figure 2, this assumption is justified by the data itself. In this section, we have shown that the measurements derived under this assumption produce physically sensible results and distributions. Comparisons of the derived gas temperatures and turbulent velocities imply that the majority of absorbers have subsonic internal gas velocities and internal energy dominated by thermal broadening.

An alternative physical scenario detailed in Stern et al. (2016) posits that CGM clouds could be highly stratified in density, with low-ionization gas resulting from the dense cores of more physically extended and more highly ionized structures. In this scenario, one might expect that the gas temperature or nonthermal motions of the different ions would also be qualitatively different such that different ionization states would look kinematically distinct. In such a scenario, the modeling assumptions made in Section 3 would not hold. However, as we argued in Section 3 and demonstrate in Figure 2, the velocity profiles of absorption lines from like-element ions with different ionization states (e.g., C II and C IV), *where well detected*, typically appear very similar, while the line shapes of heavier ions typically appear narrower than those of lighter ions (Figure 1), even when they have more similar ionization potentials (e.g., Si IV and C IV).

Note that we do not rule out the possibility that higher density cores are embedded in a more highly ionized medium. Future analysis of the ionization states of KBSS CGM absorbers will test this possibility. However, if such a model holds for the gas surrounding these galaxies, the higher density cores and surrounding outer envelopes would be modeled as separate absorbers. In fact, this model likely does describe the two phases of halo gas, one detected in O VI and C IV and the other detected in C IV and lower-ionization species. However, we detect and model these structures as separate absorption components. Section 7.2 shows observational evidence that such a scenario may be a good description of the data.

6.2. Doppler Widths of O VI Absorbers

The properties of O VI-bearing absorbers are of considerable interest given the expectation that O VI could trace a hotter gas phase, more similar to properties expected for gas heated by outflows or accretion shocks, cooling from $\log(T/{\rm K}) > 5.5$ (Heckman et al. 2002; Ford et al. 2014; Bordoloi et al. 2017; Voit 2019).

The typical O VI line width in our sample is quite broad and much broader than that of low and intermediate ions detected nearby in velocity (see Figure 3). The mean $b_{\rm d,\,O\,VI} = 23.9$ km s^{-1} and a median $b_{\rm d,\,O\,VI} = 18.3$ km s^{-1} compared with a mean C IV Doppler width of $b_{\rm d,\,C\,IV} = 12.4$ km s^{-1} and a median $b_{\rm d,\,C\,IV} = 9.3$ km s^{-1}. These values, if one assumes pure thermal broadening, correspond to O VI-bearing gas with a mean (median) temperature of $\log(T/{\rm K}) = 5.7$ (5.5) and C IV-bearing gas with $\log(T/{\rm K}) = 5.0$ (4.8). Notably, for O VI and C IV, a temperature $\log(T/{\rm K}) = 5.5$ and $\log(T/{\rm K}) = 5.0$ corresponds to the temperature at which the O^{5+}/O and C^{3+}/C ratios peak for gas in CIE.

Figure 12 compares the full distribution of $b_{\rm d}$ for O VI and C IV absorbers. It is evident from both the bulk statistics and

[19] For typical measured gas temperatures $10^4 < T < 10^6$ K, the sound speed is in the range $17 < c_s < 170$ km s^{-1}.

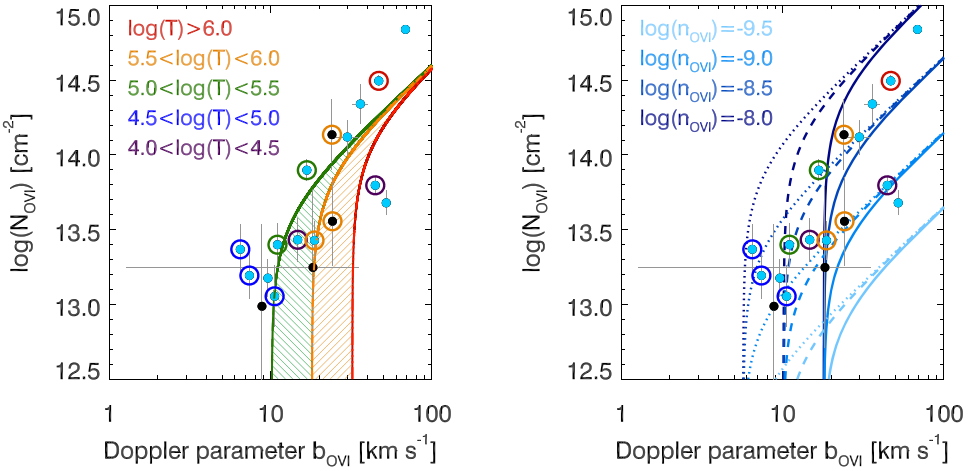

Figure 13. Measured Doppler width of O VI-bearing absorption components compared to their column densities. Absorbers plotted in light blue are $>2\sigma$ significant measurements of N. A Spearman's rho test confirms that $N_{\rm O\ VI}$ is positively correlated with Doppler width at 4.3σ significance. Absorbers with measured temperatures are surrounded by circles whose color indicates the inferred gas temperatures as labeled in the left-hand plot. The gas temperature is also positively correlated with column density, although the significance of this correlation is lower. The curves and shading show theoretical predictions for relationships between $N_{\rm O\ VI}$ and b. Plotted on the left are the cooling models from Heckman et al. (2002), who predict a relationship between $N_{\rm O\ VI}$ and b for shock-heated radiatively cooling gas with $5 \lesssim \log(T/{\rm K}) \lesssim 6$. Note that here we assume the Heckman et al. (2002) curves represent the width of *individual* absorbers, not the total velocity width of all O VI. On the right are plotted the models from Stern et al. (2018), who consider gas with $T < T_{\rm vir}$ where the motions of the O VI-bearing gas are dominated by bulk flows. In these models, the relationship is dependent on the gas density, here parameterized as the volume density of O^{5+} ions (shown in shades of blue) and the gas temperature. We plot three temperatures: $\log(T/{\rm K}) = 5.5$ as solid lines, $\log(T/{\rm K}) = 5.0$ as dashed lines, and $\log(T/{\rm K}) = 4.5$ as dotted lines.

the full distribution that the O VI gas has significantly larger Doppler parameters; however, it is of interest that there exist a sample of broad C IV absorbers as well. The large line widths and, in some cases, corresponding high temperatures suggest that many of these broad absorbers, most commonly detected in O VI and C IV, are collisionally ionized and consistent with the properties of a metal-enriched hot halo or hot gas outflow. Future ionization analysis will more fully address the origin of this gas.

Previous absorber studies have found similar trends in other environments. Fox et al. (2007a, 2007b) studied the properties of C IV and O VI absorbers associated with high-column-density H I absorbers (damped Lyman-alpha absorbers; DLAs; and sub-DLAs). They also found both narrow and broad C IV components and broad O VI absorbers they suggest were collisionally ionized. Muzahid et al. (2012) considered the full population of O VI absorbers in QSO spectra and found that the Doppler parameters of O VI absorbers were typically larger than those of C IV. Simcoe et al. (2002) measured the widths of O VI absorbers in high-z QSO spectra, finding a median $b_{\rm d,\ O\ VI} = 16$ km s^{-1}, similar to the value we find here.

Figure 13 shows the measured column densities, line widths, and temperatures of O VI absorbers in our sample. Notably, both the widths of O VI absorbers and their inferred temperatures are correlated with their column densities. A Spearman's rho test confirms that $b_{\rm d}$ and N are significantly correlated (4.3σ). The correlation between N and $b_{\rm d}$ is stronger than the correlation between N and T, even if the sample is restricted to the fraction of the sample with temperature measurements.

The correlation between $b_{\rm d}$ and $N_{\rm O\ VI}$ has been noted previously at lower redshift (see, e.g., Heckman et al. 2002; Werk et al. 2016; Bordoloi et al. 2017; Zahedy et al. 2019.) Heckman et al. (2002) and more recently Bordoloi et al. (2017) have proposed that such a correlation would be expected in the case of $T \sim 10^{5-6}$ K gas radiatively cooling behind a fast shock. The relationship predicted by these models is shown in the left-hand panel of Figure 13. The data here generally agree with the predictions from Heckman et al. (2002) when one considers the Doppler widths of *individual absorbers* rather than the velocity width of all of the O VI absorption. If this model accurately reflects the source of O VI absorbers, it is notable that the model assumes metallicities $Z/Z_{\odot} > 0.1$, suggesting the gas detected in O VI is typically quite enriched.

In the right-hand panel of Figure 13, we also compare to the model of Stern et al. (2018), who predict a relationship between $N_{\rm O\ VI}$ and b resulting from nonthermal gravitational broadening of O VI absorbers that are physically extended in size ($r \gtrsim 10$ kpc) and traveling ballistically through a dark matter halo. Such a model could hold if the gas was either falling into or flowing out of the galaxy. Absorbers in this scenario experience velocity shear due to their extended sizes, which broadens the resulting absorption features. The curves in Figure 13 show the quadratic sum of the thermal broadening for three gas temperatures [solid curves for $\log(T/{\rm K}) = 5.5$, dashed curves for $\log(T/{\rm K}) = 5.0$, and dotted curves for $\log(T/{\rm K}) = 4.5$] with this nonthermal broadening, calculated for $z = 2.3$ absorbers using Equation (21) in Stern et al. (2018). Note that the velocity shear is inversely proportional to the dynamical time of the halo, and hence generally larger at $z \sim 2$ than at $z \sim 0$. Overall, these theoretical curves appear broadly consistent with the data and offer a more compelling model for absorbers with measured $\log(T/{\rm K}) < 5$, where the Heckman et al. (2002) models are not applicable.

Alternatively, absorbers with low inferred temperatures could be overionized gas that has rapidly cooled. For initially hot gas radiatively cooling to $T \lesssim 10^6$ K, nonequilibrium ionization effects are likely due to the short cooling times at these temperatures. Rapid radiative cooling leads to the recombination of the gas lagging behind the drop in temperature, resulting in overionization of the gas compared to CIE (Gnat & Sternberg 2007; Oppenheimer & Schaye 2013; Gnat 2017).

Further analysis of this O VI-bearing gas is warranted. Any scenario attempting to explain the origin of these absorbers must explain not just their measured $N_{\rm O\ VI}$, but also their $b_{\rm d}$ and measured temperatures. Future work will more fully consider the ionization conditions within this sample, which may further elucidate the origin of this gas.

7. Discussion

7.1. Implications of the Measured Gas Temperatures

As discussed in Section 6, the thermal properties of the gas within the CGM offer direct insight into the properties of accreting and outflowing gas, constraining the physical processes affecting gas accretion and those driving galactic winds. Because of this, the temperature distribution shown in Figure 9 is of considerable interest.

The inferred temperature range of the halo gas is not unexpected given the ionization states we use to trace the CGM, which for collisionally ionized gas peak in the temperature range $4 < \log(T/{\rm K}) < 5.5$. However, the range of temperatures found is notable for a number of reasons. First, the measurements require that much of the gas within the halos of L^* galaxies at $z \sim 2$ has temperatures at which radiative cooling is most efficient (Dalgarno & McCray 1972). For such gas, the cooling time is short.[20] Given this, gas at these temperatures is expected to be short-lived unless it is subject to nearly continuous heating. Alternatively, the existence of intermediate-temperature gas could be common if such gas forms via cooling out of a more massive hot phase (Maller & Bullock 2004; McCourt et al. 2012; Scannapieco 2017; Voit et al. 2017; Schneider et al. 2018; Suresh et al. 2019).

The majority of the gas appears to be hotter than the typical temperature of hydrogen clouds within the $z \sim 2$ IGM. Inferences based on H I absorbers indicate that the IGM has a typical temperature at mean density of $\sim(1\text{–}2) \times 10^4$ K (Hui & Gnedin 1997; Schaye et al. 1999; Rudie et al. 2012a). More than one-half of the absorbers in our sample have line widths broader than expected for that temperature.

The IGM temperature is set by a balance between photoionization heating and adiabatic cooling due to the expansion of the universe. Within a galaxy's dark matter halo, the gas would not be freely expanding, so significant adiabatic cooling would be unlikely. Therefore, the equilibrium temperature in the absence of accretion shocks or heating from galactic winds would be set by the balance of photoionization heating and radiative cooling. Around the mean cosmic density at $z \sim 2$, this equilibrium temperature is insensitive to metallicity and reaches as high as 2×10^5 K (Smith et al. 2017). However, the expected gas density within galaxy halos is significantly higher than the mean density of the universe. At higher densities, the equilibrium temperature drops such that at 100 times the mean density (still lower than the typical dark matter density within the halo), $T_{\rm equ} \approx 5 \times 10^4$ K with only a modest dependence on metallicity.

While much of the gas is hotter than random places in the IGM and hotter than expected for photoionization heating, the temperature of almost all of the gas we detect is lower than the virial temperature of the halo in which it resides. The virial temperature of a dark matter halo of virial radius $R_{\rm vir}$ and halo mass $M_{\rm halo}$ is defined to be

$$T_{\rm vir} = \frac{\mu m_{\rm p} G M_{\rm halo}}{2 R_{\rm vir} k}, \tag{8}$$

where $\mu = 0.6$ is the assumed mean molecular weight, $m_{\rm p}$ is the proton mass, and k is the Boltzmann constant. Assuming the typical halo mass and virial radius for the sample, $M_{\rm halo} = 10^{11.9}\ M_\odot$ and $R_{\rm vir} = 90$ kpc (Trainor & Steidel 2012), the typical virial temperature for the galaxies in this sample is $T_{\rm vir} \approx 10^6$ K.

At $T \sim 10^6$ K, we expect collisional ionization to be dominant and C IV and Si IV to be poor tracers of the gas since most C and Si would be more highly ionized. Even O VI, which has the highest ionization potential of any of the ions we can currently measure, peaks in CIE at $T = 10^{5.5}$ K. Thus, these measurements do not preclude the existence of gas with $T \gtrsim 10^6$ K within the halos of these galaxies. However, the data do require a substantial reservoir of gas at intermediate temperatures.

The data presented are not at odds with the picture of cold flows of filamentary accretion. Roughly one-half of the absorbers are cool with $T = 10^4\text{–}10^{4.5}$ K. However, given that much of the gas is hotter than is typical within the IGM, it is clear that additional heating is present. The intermediate temperature of much of the gas within the CGM is concrete evidence that the gas is affected by its proximity to the galaxy, most likely through shock heating during accretion or via galactic winds, with much of the intermediate-temperature gas likely resulting from cooling.

As the thermal state of CGM gas is directly tied to the physics of outflows or accretion shocks, it is likely that these measurements are a powerful diagnostic that should be used to constrain physical models implemented in hydrodynamic simulations. Ideally, such simulations would report the temperature distribution of gas weighted by its ionic column densities, or other analogous quantities that can be compared directly with this data set. In the absence of such predictions, we compare here to temperature distributions made for the mass of gas and metals within the halo of simulated galaxies. Given that we do not measure directly the mass of the gas or metals in these observations, these comparisons should be viewed as exploratory rather than conclusive.

Muratov et al. (2017) and Hafen et al. (2019) analyzed the temperature distribution of gas within $R_{\rm vir}$ of galaxies at $z = 2\text{–}2.5$ in the FIRE simulations. Muratov et al. (2017) report the fraction of metal mass as a function of temperature in three simulations with stellar masses $M_* = 10^{9.5}\ M_\odot$ at $z > 2$. They find less than 20%–30% of the metal mass has $T > 10^{4.7}$ K, with roughly 60% of the metals having $10^4 < T < 10^{4.7}$ K. Considering galaxies with halo masses $M_{\rm halo} = 10^{11.5}\ M_\odot$, Hafen et al. (2019) found that 40%–50% of the total CGM gas mass (including hydrogen) is cool [$4 < \log(T/{\rm K}) < 4.7$] and another 40%–50% is hot [$\log(T/{\rm K}) > 5.3$], with less than 10%–20% of the gas having warm gas temperatures [$4.7 < \log(T/{\rm K}) < 5.3$].

While we cannot constrain the *mass fraction* of gas as a function of temperature, over one-half (61% by number) of the absorbers in our sample have $\log(T/{\rm K}) < 4.7$; 20% of absorbers in our sample with measured temperatures would be classified as warm [$4.7 < \log(T/{\rm K}) < 5.3$],[21] and 17% of

[20] The precise cooling time of gas is determined by its density and metallicity; however, for all gas with densities higher than the mean density at $z \sim 2$, the cooling time for $T = 10^5$ K is less than 10^8 yr. For the somewhat higher densities expected in the CGM, and for higher metallicities, the cooling time decreases substantially.

[21] If we include absorbers with upper limits on their temperature, this fraction is unchanged.

the absorbers have line widths or measured temperatures consistent with hot gas [$\log(T/\mathrm{K}) > 5.3$].

The measured KBSS values *weighted by number of absorbers* are similar to those presented by Muratov et al. (2017) averaging by metal mass, but there appears to be a somewhat larger fraction of gas with $\log(T/\mathrm{K}) > 4.7$ in the KBSS galaxy halos than was found by Muratov et al. (2017). Alternatively, presuming that we are missing some fraction of the hot absorbers because they do not produce detectable absorption in the observed ions, the observed temperature distribution of absorbers *weighted by number* appears roughly consistent with the *mass-weighted* fractions reported by Hafen et al. (2019). Given that it is unlikely that the mass-weighted and number-weighted temperature distributions are the same, additional analysis of the simulations may allow for better comparisons with the data in the future.

Fielding et al. (2017) considered idealized high-resolution simulations of galactic halos to study the thermal properties of gas around galaxies and how they are affected by inflows and outflows. Depending on the details of the feedback efficiency used, the simulations showed significant differences in the quantity of gas at intermediate temperatures [$4.5 < \log(T/\mathrm{K}) < 5.5$]. Importantly, the halos that showed this effect were ∼0.5 dex lower in mass than the halos considered here; however, the higher-mass halos showed less variation, due to the predominance of thermal support from a hot halo. One caveat in the comparison is that the simulations were initialized with a hot halo of gas at $T = T_{\mathrm{vir}}$, which is unstable at $\log(M_{\mathrm{halo}}/M_{\odot}) < 11.5$, but stable for galaxies in the mass range of the KBSS. However, if the KBSS galaxies have not yet built a stable and massive hot halo, perhaps the intermediate-temperature gas in KBSS halos is also particularly sensitive to feedback. If so, the temperature distribution of KBSS halo gas may be a critical probe of properties of galactic outflows within galaxies in the distant universe. This possibility should be investigated further.

Recently, several studies have focused on the existence of cool ($T \sim 10^4$ K) and warm ($T \sim 10^5$ K) gas in galactic winds. The measurements here provide a critical test of these outflow models. In most detailed models, galaxies drive out hot ($T > 10^6$ K) gas, rapidly shredding any embedded cold clouds via Kelvin–Helmholz instabilities. However, in some models, comoving cold gas grows in mass or is re-formed via radiative cooling instabilities (Thompson et al. 2016; Scannapieco 2017; Gronke & Oh 2018; Schneider et al. 2018). Another class of models drive galactic winds via cosmic-ray pressure. Recent theoretical work has shown that winds driven by cosmic rays are cooler (Booth et al. 2013; Girichidis et al. 2018) and that the overall mass with $T < 10^5$ K in the low-redshift CGM is substantially increased (Salem et al. 2016). Salem et al. (2016) and Butsky & Quinn (2018) showed that the thermal structure of the CGM is highly sensitive to both the mode and detailed treatment of cosmic-ray transport (advective streaming versus isotropic or anisotropic diffusion). Clearly, the data presented herein can test or constrain many aspects of these models; however, such a comparison requires detailed predictions from simulations that are matched to the properties we can observationally constrain (column densities of observed ions, ion-weighted temperatures, projected velocities). More detailed comparisons should be made between these and other outflow models and these observations.

7.2. Constraints on Sizes of Absorbers within the Halo

Another interesting consideration is the low measured turbulent broadening of the gas. The distribution in Figure 10 provides useful constraints for theoretical models and simulations attempting to explain or reproduce observations of the CGM. In particular, many recent theoretical studies have focused on the small-scale structure within the CGM, suggesting that the CGM may be made up of very small clouds, more analogous to a terrestrial fog or mist (Voit et al. 2017; Hummels et al. 2019; Liang & Remming 2018; McCourt et al. 2018). Depending on the true size scale of such "cloudlets" and whether they are smaller or larger than the projected size of the background QSO at the location of the cloud (sizes as small as, or smaller than, 10^{-4}–10^{-2} pc; Dai et al. 2010; Morgan et al. 2010; Jiménez-Vicente et al. 2014; Mudd et al. 2018), each component of our Voigt profile fit corresponds either to a single cloudlet or a coherent aggregate of such structures. In the former scenario, these observations constrain the turbulence of gas within single cloudlets. In the latter, they represent the velocity dispersion of the cloudlets within a single kinematically coherent structure, and the number of detected components gives an indication of the volume filling of such structures.

Our measurements suggest that internal turbulence within coherent gas structures in the halo is subdominant energetically compared to the thermal energy for over 80% of the metal-bearing absorbers. This limits the number of cloudlets that can be contained within a single absorber fit with one Voigt profile (McCourt et al. 2018).

However, the data also do not show any evidence of partial covering of the QSO beam. Multiple transitions in various galaxy halos are saturated, with absorption lines reaching zero transmission, suggesting no light passes from the background QSO unattenuated. Similarly, there is no evidence for doublet ratios inconsistent with the values set by their atomic parameters, as would be expected if only part of the QSO beam were intercepting gas along the line of sight. Given these observations, if the cloudlets are smaller in size than the QSO beam, a sufficiently large number must always be created to cause 100% areal covering fractions within the coherent gas structure, even if the volume filling factor is substantially lower.

Within the KBSS sample, we have one unambiguous constraint on the size scale of metal absorbers. One of the QSOs in our sample, Q0142 (UM673), is lensed by a foreground $z = 0.49$ galaxy (Surdej et al. 1987), producing two images separated by 2.″2, one roughly two magnitudes fainter than the other (Smette et al. 1992). We obtained Keck/HIRES spectra of both images, as discussed in Cooke et al. (2010), as well as data drawn from the Keck archive and discussed in Rauch et al. (2001). These two spectra constrain the coherence of halo absorbers at 75 kpc from one of the $z > 2$ KBSS galaxies, BX182. Following the calculations in Cooke et al. (2010), we derive a separation of the two sight lines of ∼400 pc at the redshift of Q0142-BX182. We note that these spectra were analyzed by Rauch et al. (2001) to study the coherence scale of IGM metal absorbers (see their Figure 1, right-hand panel). Here we only consider those absorbers within ±1000 km s^{-1} and 100 kpc of Q0142-BX182.

Figure 14 shows a comparison of the Voigt profile fit to the spectrum of UM673A (colored curves) compared to the spectrum of UM673B (black spectrum), which probes the gas

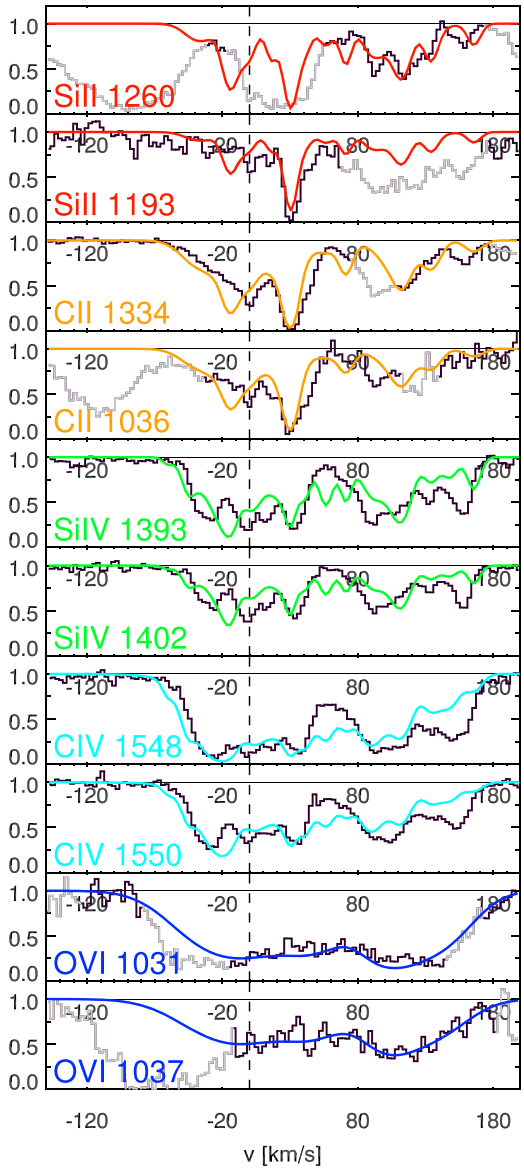

Figure 14. Constraints on the size scale of absorbers within the halo of Q0142-BX182 from a lensed background QSO. The colored curve shows the Voigt profile fit to the brighter image (UM673A) of Q0142. The black spectrum is the continuum-normalized spectrum of the second image (UM673B) of the QSO, which probes the halo gas 400 pc from the brighter image. Notably, the overall velocity spread of the gas is nearly identical across the two sight lines, suggesting that the metal-enriched structure giving rise to these absorbers spans distances $\gg$ 400 pc. Similarly, the O VI spectrum appears unchanged across this distance range; however, the detailed structure within all of the lower-ionization gas (including C IV) has significant differences between the two sight lines, suggesting individual clouds or density inhomogeneities within the halo typically have sizes <400 pc. As in Figure 3, the gray sections of the spectrum show regions of contamination within the spectrum.

400 pc from the A sight line. Overall, the velocity range covered by metal-enriched gas is constant across the two sight lines, suggesting the metal-enriched structure responsible for the metal absorption within the halo of Q0142-BX182 is larger than 400 pc. The O VI section of the spectrum appears completely consistent between the two sight lines, suggesting there are no significant differences in velocity or density within the O VI-bearing phase on such small scales.

Conversely, the detailed subcomponent structure in the lower-ionization gas (including C IV) shows significant differences between the two lines of sight: the strengths, widths, and centroids of the various components are typically different between the two sight lines. Some absorbers, such as the strong low-ionization absorber at $v \sim 30$ km s^{-1}, appear unchanged between the two sight lines; however, most have noticeable differences. This suggests that the majority of halo clouds (or coherent cloudlet structures) are smaller than (or have density variations on scales comparable to) the sight-line separation, 400 pc, while the overall structure containing metal-enriched gas within the halo is much larger, consistent with the conclusions of other absorber studies with lensed QSOs (Rauch et al. 2001; Adelberger et al. 2005; Chen et al. 2014; Zahedy et al. 2016). Further, these patterns imply that the O VI-bearing gas likely is more volume filling than the lower-ionization gas.

7.3. Comparison of Derived Temperature and Gas Turbulence to Low-redshift CGM Measurements

Zahedy et al. (2019) compared the Doppler parameters of Mg II and H I absorbers within the inner CGM of massive elliptical galaxies at $z \sim 0.4$. These authors report that the low-ionization CGM has a mean temperature of 2×10^4 K, similar to typical IGM temperatures and cooler than we have found here. The measured turbulence within these Mg II absorbers was similar to that found in our sample with $v_{\rm turb} = 7 \pm 5$ km s^{-1}.

Similar to Rudie et al. (2012b), Tumlinson et al. (2013) used the measured Doppler widths of H I absorbers in the CGM of galaxies in the COS-Halos survey to measure an upper limit on the temperature of H I-bearing gas of $\log(T/{\rm K}) \lesssim 5.3$ K assuming pure thermal broadening. Compared to IGM samples of H I absorbers selected without knowledge of the positions of galaxies (Thom & Chen 2008; Tripp et al. 2008; Tilton et al. 2012), Tumlinson et al. (2013) found that the CGM b-parameter distribution was consistent with that of the full IGM; that is, they do not find that H I absorbers in the low-z CGM are characteristically different from the full distribution of IGM absorbers, even for gas surrounding the massive early-type population (Thom et al. 2012).

Both Thom et al. (2012) and Tumlinson et al. (2013) note that the inferred gas temperature is less than the virial temperatures of the expected dark matter halos of the COS-Halos galaxies; however, they note that this result is unsurprising given that the tracer is neutral (H I) and that broad absorbers consistent with million-degree gas are very challenging to detect, especially when blended with the narrower H I absorption commonly found surrounding COS-Halos galaxies.

7.4. Comparison of Derived Temperature and Gas Turbulence to Other Measurements in the IGM

The measurements presented herein are not the first constraints on the temperature and turbulence of gas in the distant universe. Several studies have focused on the thermal and turbulent properties of absorbers in high-z QSO sight lines, henceforth referred to as "IGM" absorbers. Importantly, the analyzed absorbers were detected in ionized metal species (a requirement because the ratio of the widths of those lines is used to measure the temperature and nonthermal motions in the gas). Given that metals originate within stars and galaxies, these absorbers do trace a biased sample compared to general H I absorbers. Without knowledge of the galaxy distribution

surrounding these "IGM" absorbers, it is not possible to say what fraction of them are actually within the CGM of a galaxy like the ones in our sample, or any galaxy. But it is important to recognize the likelihood that they do not, as a sample, represent completely random locations within the IGM.

The first measurements of the thermal and nonthermal broadening measurements for a large sample of $z \sim 3$ IGM absorbers were reported in Rauch et al. (1996). These authors considered a sample of 79 C IV absorbers with detected Si IV and found a mean $b_{\rm d,\,C\,IV} = 12.6$ km s^{-1} and a median $b_{\rm d,\,C\,IV} = 9.6$ km s^{-1}. In our CGM sample, we find a mean $b_{\rm d,\,C\,IV} = 12.4$ km s^{-1} and a median $b_{\rm d,\,C\,IV} = 9.3$ km s^{-1}, in complete agreement with the values reported by Rauch et al. (1996). Decomposing the Doppler widths into thermal and nonthermal components, Rauch et al. (1996) found a typical $v_{\rm turb} = 6.3$ km s^{-1}, slightly smaller but consistent with our derived measure of turbulence. Similarly, they derive a typical temperature of 4×10^4 K, consistent with the median values shown in Figure 9.

More recently, Kim et al. (2016) used a sample of 54 kinematically simple C IV and C III $2.1 < z < 3.4$ IGM absorbers for which the associated H I absorption could be isolated. By comparing the $b_{\rm d}$ parameters of the C and H absorbers, these authors derive gas temperatures with a mean of $\langle \log(T/{\rm K}) \rangle = 4.27 \pm 1.0$ and median $\log(T/{\rm K}) = 4.47$, again consistent for the values found within the CGM.

Both of these comparisons imply significant similarities between the typical metal-bearing absorber selected at random from a QSO line of sight ("IGM" absorber) and the typical metal-bearing absorber known to be within the CGM of a galaxy with $z > 2$. While the temperature of gas within the CGM typically appears to be higher than random H I absorbers within the IGM, it is similar to that of metal-bearing IGM gas. Given that all metals within the IGM must have once passed through or still be contained within the CGM of some galaxy, this conclusion is not surprising. However, given the very rapid cooling time of gas at the intermediate temperatures that compose one-half of the detected gas, this may suggest that a nonnegligible fraction of IGM absorbers at $z \sim 2$–3 have been ejected from or in some other way heated by a galaxy in the recent past.

7.5. Metal Mass in the High-redshift CGM

We close with a rough estimate of the metal mass detected within the halo of KBSS galaxies. We calculate the implied mass in metals using the total column densities ΣN and covering fractions f_c measured in Section 4. We begin by calculating the measured mass in each ion:

$$M_{\rm ion} = \pi D_{\rm max}^2 \, m_{\rm ion} \, f_c \, \langle N_x \rangle, \quad (9)$$

where $D_{\rm max}$ is the maximum impact parameter at which the ion is measured in the sample, $m_{\rm ion}$ is the mass of the ion, f_c is the covering fraction of the ion measured within $D_{\rm max}$, and $\langle N_x \rangle$ is the average column density measured across the detected sample. We note that for C III, Si III, Si IV, and C IV, many of the measured ΣN are lower limits. We treat them as detections in the average, so the values reported here are lower limits on the mass within the halo.

Table 3 shows the measured values for these parameters and the implied mass in each ion within $R_{\rm vir}$, which corresponds to $10^{5-6}\ M_\odot$ for each ion. For photoionized gas, we would expect to detect the majority of the phases of Si and C within this sample, so we sum the measured Si II, Si III, and Si IV as well as the measured C II, C III, and C IV to find the total metal mass within the photoionized phase: $M_{\rm Si,photo} \geqslant 10^{5.7}\ M_\odot$ and $M_{\rm C,photo} \geqslant 10^{6.1}\ M_\odot$.

Table 3
Metal Mass within the Halo

Ion	min(log(N_x))[a] (cm^{-2})	$D_{\rm max}$[b] (pkpc)	f_c	log($\langle N \rangle$)[c] (cm^{-2})	log(M_x) ($M_\odot$)
Si II	12.6	75	0.6	13.85	5.2
C II	12.4	75	0.6	14.46	5.5
Si III	···	90	1.0	13.23	5.0
C III	···	90	1.0	14.20	5.6
Si IV	···	90	1.0	13.62	5.4
C IV	···	90	1.0	14.31	5.7
O VI	···	75	1.0	14.80	6.2
Total C	···	···	···	···	6.1
Total Si	···	···	···	···	5.7
Total O[d]	···	···	···	···	6.9

[a] For ions with nondetections within $D_{\rm max}$, the minimum column density detectable in all sight lines.
[b] The impact parameter of the farthest galaxy in the sample that has a detection of the ion.
[c] The mean column density among the detections.
[d] The total oxygen mass calculated assuming 20% of oxygen is in the state O^{5+}. See text for more details.

For oxygen, we only detect the highly ionized O VI stage. O VI traces <20% of the oxygen, regardless of the ionization mechanism (Tumlinson et al. 2011; Oppenheimer & Schaye 2013), so the total oxygen within the phase traced by O VI is at least 5 times larger: $M_{\rm O,hot} \geqslant 10^{6.9}\ M_\odot$. However, this is a conservative upper limit on the O^{5+}/O fraction. For photoionized O VI at lower gas temperatures, O^{5+}/O typically remains below 10%. In CIE, the O^{5+}/O fraction is strongly peaked at $10^{5.5}$ K and declines sharply at higher and lower temperatures, with $O^{5+}/O < 1\%$ at $T = 10^6$ and $T = 10^5$ K (see Oppenheimer & Schaye 2013). Therefore, the mass of oxygen traced by the detected O VI could be significantly more substantial.

To place these values into context, we compare the total mass in each ion with the mass of that element we expect to have been produced by a typical KBSS galaxy, as well as the observed mass of metals contained within the ISM and locked in stars, as shown in Table 4.

We begin with an estimate of the total amount of metals produced by the galaxy. The initial mass function (IMF)-weighted yields of a stellar population carry significant uncertainties. These are driven by uncertainties in the IMF itself and by assumptions about the highest-mass stars that contribute to nucleosynthesis and, to a lesser extent, the effect of rotation and mass loss in massive stars and uncertainties in the yields of individual supernovae (Vincenzo et al. 2016). These uncertainties propagate into nearly an order of magnitude uncertainty in the total yield of a given stellar population. Reasonable assumptions can lead to values that range from 0.006 $M_\odot$ of oxygen for every $M_\odot$ of stars formed (Nomoto et al. 2006) to upwards of 0.03 $M_\odot$ and potentially even higher from top-heavy IMFs (Vincenzo et al. 2016). Given the large uncertainty, we choose as a fiducial value 0.015 $M_\odot$ of oxygen for every solar mass formed, as this value has commonly been assumed in previous CGM studies (Tumlinson et al. 2011; Peeples et al. 2014; Johnson et al. 2017), but we caution again that this value is highly uncertain.

Table 4
Metal Mass in Galaxies

Location	$\log(M_C)$ $(M_\odot)$	$\log(M_{Si})$ $(M_\odot)$	$\log(M_O)$ $(M_\odot)$
Photoionized halo gas	>6.1	>5.7	···
O VI-bearing halo gas	···	···	>6.9
ISM	7.1	6.7	7.7
Locked in stars	7.2	6.8	7.8
Produced by the stars	8.0	7.6	8.6

The mean stellar mass of the KBSS galaxies in this sample is $\langle M_* \rangle = 10^{10.3}\ M_\odot$ (Strom et al. 2017). For a 100 Myr old stellar population, the total mass of stars formed is roughly 1.4 times the current stellar mass[22] for a Chabrier (2003) IMF (Bruzual & Charlot 2003). Thus, we expect a typical galaxy in our sample to have formed $10^{10.4}\ M_\odot$ of stars and $10^{8.6}\ M_\odot$ of oxygen. Using either the solar abundances from Asplund et al. (2009) or the core-collapse supernova yields from Woosley & Heger (2007) or Nomoto et al. (2006), the Si/O mass fraction is ∼0.1, implying $10^{7.6}\ M_\odot$ of Si. The nucleosynthetic origin of carbon is more complex, and the C/O mass fraction ranges from ∼0.1 to 0.5. We select C/O = 0.25 as it is in the middle of this range and is the value measured within ionized H II regions within KBSS galaxies (Steidel et al. 2016). Using this value implies an assembled mass of $10^{8.0}\ M_\odot$ of C.

This suggests that within the halo we have only detected ∼1%–2% of the O, C, and Si formed by the stellar population, although with large uncertainties dominated by uncertainties in the IMF-weighted yields.

We can also compare the halo metal mass to an estimate of the metal mass found within the ISM of these galaxies. Tacconi et al. (2010) measured the gas mass in typical star-forming galaxies at $\langle z \rangle = 2.3$, finding that the cold ISM contained 44% of the total baryonic mass within the galaxy [$M_{gas}/(M_{gas} + M_*) = 0.44$], implying $M_{ISM} = 10^{10.2}\ M_\odot$ for the KBSS galaxies in our sample. The abundance ratios within the molecular gas are not well constrained by the Tacconi et al. (2010) data, so instead we rely on abundances derived from nebular emission from H II regions. Since the massive stars are formed out of molecular gas within these galaxies, we assume for this estimate that the abundances are similar in the ionized, neutral, and molecular phases. Strom et al. (2018) report that KBSS galaxies have a median gas-phase oxygen abundance 12 + log(O/H) = 8.37,[23] implying an oxygen mass within the ISM of $M_{O,ISM} = 10^{7.7}\ M_\odot$. We assume the same abundance ratios as were discussed above to estimate the carbon and silicon ISM masses, finding $M_{O,ISM} = 10^{7.1}\ M_\odot$ and $M_{Si,ISM} = 10^{6.7}\ M_\odot$. Comparison of these values with the total yields calculated above suggests that the ISM of KBSS galaxies has retained ∼10% of the metals formed.

Rounding out the census of observed metals are those locked within stars at the time of observation. To estimate the metal mass in stars, we assume all stars in the galaxy have the same abundance as the ISM. We use the same abundance ratios as above and the average stellar mass to calculate $M_{O,star} = 10^{7.8}\ M_\odot$, $M_{C,star} = 10^{7.2}\ M_\odot$, and $M_{Si,star} = 10^{6.8}\ M_\odot$.

Our very conservative lower limit on the total oxygen in the highly ionized O VI phase within 75 kpc is 15% of the ISM oxygen. The lower limit on the carbon and silicon in the photoionized phase is 10% of the ISM carbon and silicon mass. The kinematic structure of the various ions implies that O VI traces a distinct phase of gas compared to the likely photoionized Si and C; therefore, the masses that they trace are also distinct. If we assume the abundance pattern is similar in the photoionized and O VI-bearing phases, we can add their ISM fractions, suggesting we are tracing a total metal mass within the halo equivalent to >25% of the ISM metal mass and plausibly a considerably larger fraction.

While the detected halo metal mass is sizable, these calculations suggest we may have yet to account for the majority of the metals formed by the galaxy. Given the uncertainties in the total metal yields discussed above, it is plausible that a factor of a few or larger error exists in these calculations, and that the majority of the metals produced are actually accounted for. However, it is also possible that a large fraction of the metals are yet to be observed. If so, where are these metals?

The data analyzed here are not particularly sensitive to hot gas with $T \gtrsim 10^6$ K, so it is possible that a significant fraction of the metals are too hot to be studied via UV absorption. Further, ∼90% of our sample is probed at $D_{tran} > 0.5R_{vir}$, with only one low-mass galaxy probed at smaller separations. Therefore, it is plausible that the column densities of metals are larger within the inner CGM, allowing for a substantial fraction of the metals to still lie within the halo.

An additional possibility, however, is that a large fraction of the metals made by the system are now at distances $>R_{vir}$. Among KBSS galaxies with unbound C IV, at least 20% of the C IV column density is unbound, so it is plausible that a sizable fraction of the metals formed within the galaxy leave the halo. Indeed, KBSS galaxies show significant column densities of C IV and relatively high covering fractions at much larger distances (G. C. Rudie et al., in preparation). Rudie et al. (2012b) found significant enhancement in H I to 300 pkpc. If much of this gas is also metal enriched, it could correspond to a significant reservoir of metals. Given that 70% of galaxies in this sample with detected metals have some unbound metal-enriched gas, it appears likely that some fraction of the assembled metal mass lies outside of R_{vir}. Future measurements from the KBSS sample will help to address the mass of metals beyond R_{vir}.

8. Summary

In this paper, we have presented detailed measurements of the column densities, kinematics, and internal energy of metal-bearing gas within 100 pkpc (∼R_{vir}) of eight L^*_{UV} galaxies at $z \sim 2$. These measurements are based on detailed modeling of high-resolution and high-S/N background QSO spectra, which provide the first detailed view of the properties of gas within the halo of typical high-redshift galaxies. Our findings are as follows:

1. The high-redshift CGM is multiphase. Singly, doubly, and triply ionized species typically share the same complex kinematic structure (Figure 3 and Section 3). However, an additional phase of gas is commonly detected in broad O VI and C IV. This gas is found at velocities with respect to the galaxy systemic redshifts that are similar to the narrow lower-ionization gas; however, its kinematic structure is characterized by much broader absorption features (Figure 12), consistent with a possible hot, metal-enriched wind.

[22] After 100 Myr, (1.4−1.0)/1.4 ≈ 30% of the mass in the stellar population has been returned to the ISM via stellar winds or supernova ejecta.
[23] Note that this is a fraction by number, not by mass.

2. The CGM gas is kinematically complex (Figure 3) with >10 absorption components commonly found per galaxy (Section 4 and Table 2).
3. The covering fraction of metal ions within 100 pkpc of high-z galaxies is high (Figures 5 and 6, Section 4). For column densities of $\sim 10^{12}$ cm^{-2}, the covering fraction for doubly and triply ionized species is 87%–100%. For C IV, the covering fraction is above 50% for column densities $N_{\rm C\ IV} \geqslant 10^{13.5}$ cm^{-2}.
4. O VI is challenging to measure in the high-z CGM because of H I contamination; however, when the relevant spectral range is free of contamination, we invariably find $N_{\rm O\ VI} > 10^{13.9}$ cm^{-2} (Figures 5 and 6, Section 4.4).
5. A total of 70% of galaxies with detected metal absorbers have some gas that is unbound from the halo (Figure 7, Section 5). Unbound absorbers are detected in all species (Si II–O VI, Figure 8), suggesting this gas is multiphase; however, the unbound gas is more commonly detected in high-ionization transitions. Further, unbound metals are not commonly associated with high H I column densities, suggesting the absorbers are likely highly ionized, metal-rich, or both. Given their high velocities and high levels of enrichment or ionization, a plausible origin for this material is galactic winds. In this scenario, this gas represents metal-enriched material that would be permanently removed from the galaxy.
6. The widths of absorbers of elements with different atomic masses constrain the temperature and nonthermal motions of gas within the CGM (Figure 1, Section 6). The data support a model in which single gaseous structures harbor ions of various ionization potentials from Si II–C IV (Section 3.2 and Figure 3). Where detected in the data, we model all ionization states of each absorber velocity component using a single temperature and turbulent velocity. The typical inferred gas temperature within the CGM is $T = 10^{4.3–5.0}$ K depending on the sample used (Figure 9). Roughly one-half of the detected gas has intermediate temperatures $10^{4.5} < T < 10^{5.5}$ K, hotter than the IGM, but cooler than the expected virial temperature of halos with $M_{\rm halo} = 10^{12}\ M_{\odot}$. Gas at these temperatures has short cooling times, so its persistence requires constant reheating or replenishment of the warm gas phase (Section 7.1). This gas may provide important clues about the nature of inflows and outflows at high redshift.
7. Nonthermal motions in the halo gas are low ($\langle v_{\rm turb} \rangle <$ 6 km s^{-1}, Figure 10, Section 6) and are nearly always subdominant energetically (Figure 11). Thermal energy contributes >90% of the total internal energy in 58% of the measured absorbers. A total of 80% of absorbers with measured gas temperatures and turbulence have subsonic internal gas motions. However, the velocity offset of many of the absorbers from the systemic redshift of the galaxy is large (Figure 7, Section 5). If these absorbers are located within the halos of KBSS galaxies, these CGM structures are moving through the halo with supersonic bulk velocities.
8. Most of the detected gas within the CGM appears to be warmer than is typical of H I absorbers within the IGM; however, there are few differences between the measured temperature distribution of metal-bearing absorbers in IGM samples (Rauch et al. 1996; Kim et al. 2016) and those CGM absorbers presented here, suggesting that many metal-rich absorbers in the high-z IGM have recently been heated or ejected from a galaxy (Section 7.4).
9. Observations of one halo probed by two images of a background lensed QSO suggest the overall structure of halo gas that gives rise to metal absorbers has a physical size >400 pc. O VI-bearing gas within these structures appears to be homogeneous, while C IV and lower-ionization gas exhibit variations in density and velocity structure on these scales (Section 7.2 and Figure 14). This suggests that metal-enriched zones within the halo likely have size scales of kiloparsecs or larger but with significant internal structure that varies on smaller scales. The O VI-bearing phase appears to be more volume filling than the lower-ionization gas.
10. The inferred mass of metals within the halo is large, equivalent to >25% of the metal mass within the ISM (Section 7.5). However, the estimated halo+ISM+stellar metal mass may account for less than 50% of the mass of metals formed by the stellar populations, depending on the true values of the IMF-weighted yields, suggesting that many of the metals may reside in unprobed regions or phases of the CGM.

This work represents the first detailed characterization of metal-enriched gas within the halos of high-redshift L^* galaxies; however, much more information is needed.

Given the measured temperatures of gas in the CGM of KBSS galaxies, we expect the densest and most metal-rich regions to have a rich emission line spectrum from the many UV transitions that dominate the cooling of warm, collisionally ionized gas. Ongoing observations with the Keck Cosmic Web Imager (Morrissey et al. 2018) have sufficient sensitivity to detect such emission from KBSS galaxies.

Future analysis of the data presented in this work will address the ionization conditions and abundance patterns within the CGM, providing additional data on the nature of halo gas. The KBSS data also constrain the distribution of metal absorbers on larger scales and allow for the first detailed measurements of the evolution of the metal content of the CGM as a function of redshift. Forthcoming work will address these important issues.

We thank collaborators K. Adelberger, M. Bogosavljević D. Erb, N. Konidaris, D. Law, O. Rakic, and M. Turner for their contributions to the KBSS survey. The authors thank D. Fielding, J. Stern, S. Johnson, A. Benson, A. Piro, A. Newman, M. Rauch, H.-W. Chen, F. Zahedy, E. Schneider, M. Gronke, J. Kollmeier, S. Garrison-Kimmel, and the anonymous referee for useful discussions that shaped the content or direction of this manuscript. We also wish to acknowledge the staff of the W.M. Keck Observatory, whose efforts ensure the telescopes and instruments perform reliably. Further, we extend our gratitude to those of Hawaiian ancestry on whose sacred mountain we are privileged to be guests. Early phases of this work were supported by NSF through grants AST-0908805 and AST-1313472. This research has made use of the Keck Observatory Archive (KOA), which is operated by the W.M. Keck Observatory and the NASA Exoplanet Science Institute (NExScI), under contract with the National Aeronautics and Space Administration. This work was completed in part at the Aspen Center for Physics, which is supported by National Science Foundation grant PHY-1607611.

Facility: Keck (LRIS).

Software: VPFIT, Grackle (Smith et al. 2017).

Appendix

In Figures 15–23, we present the Voigt profile fits to the data for the six remaining galaxies with detected metal absorption not shown in Figure 3. Note the significant variation in the complexity of the absorbers and their subcomponent structure.

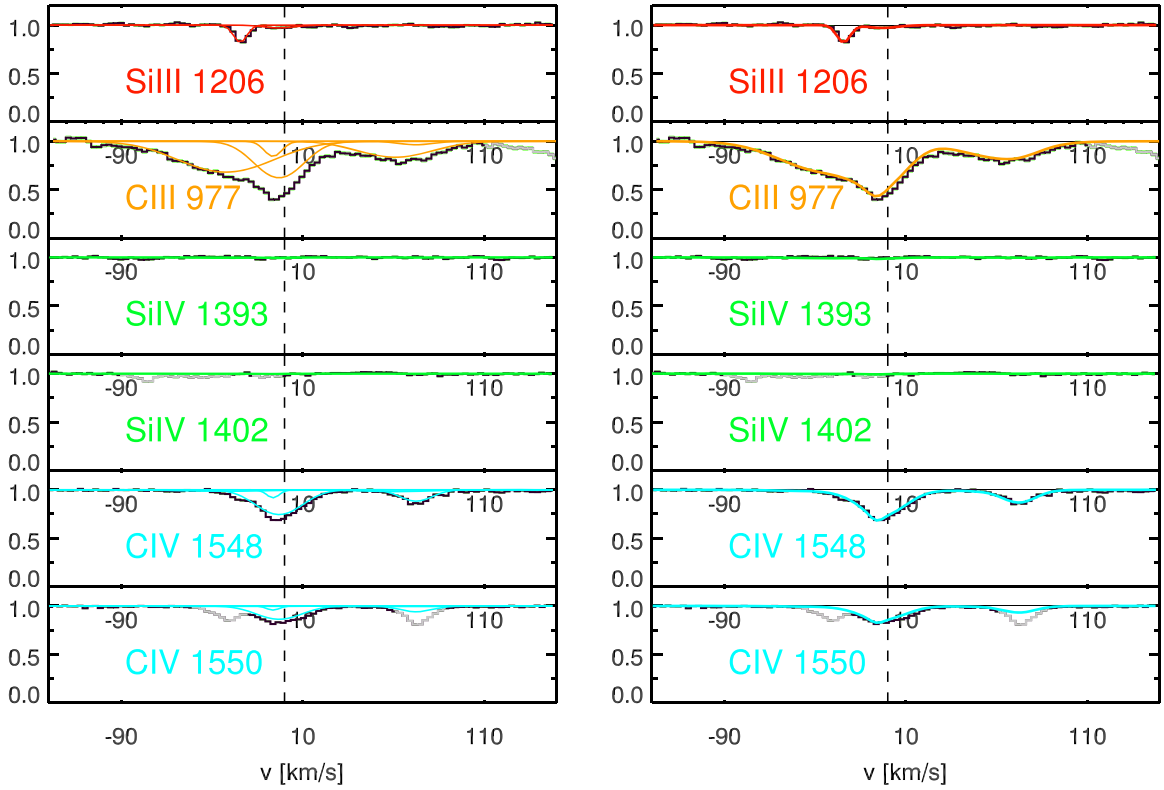

Figure 15. Example of the multicomponent absorption structure within the halo of Q0105-BX90b for the velocity range $-130 < v < 150$ km s^{-1}. The velocity scale is given with respect to the systemic redshift of the galaxy, measured based on strong rest-frame optical emission lines (Hα, [O III]). The continuum-normalized QSO spectrum is shown in black. The green curves that trace the black QSO spectrum with little to no deviation indicate the $\pm 1\sigma$ error on the normalized flux. Gray sections of the QSO spectrum are highlighted to show regions where there is contamination from H I or other metal ions within the wavelength range fit. Colored curves show the Voigt profile decomposition of the absorption. The left-hand panel shows the individual component structure, while the right-hand panel shows their product, which can be used to compare directly to the data to test the goodness of fit.

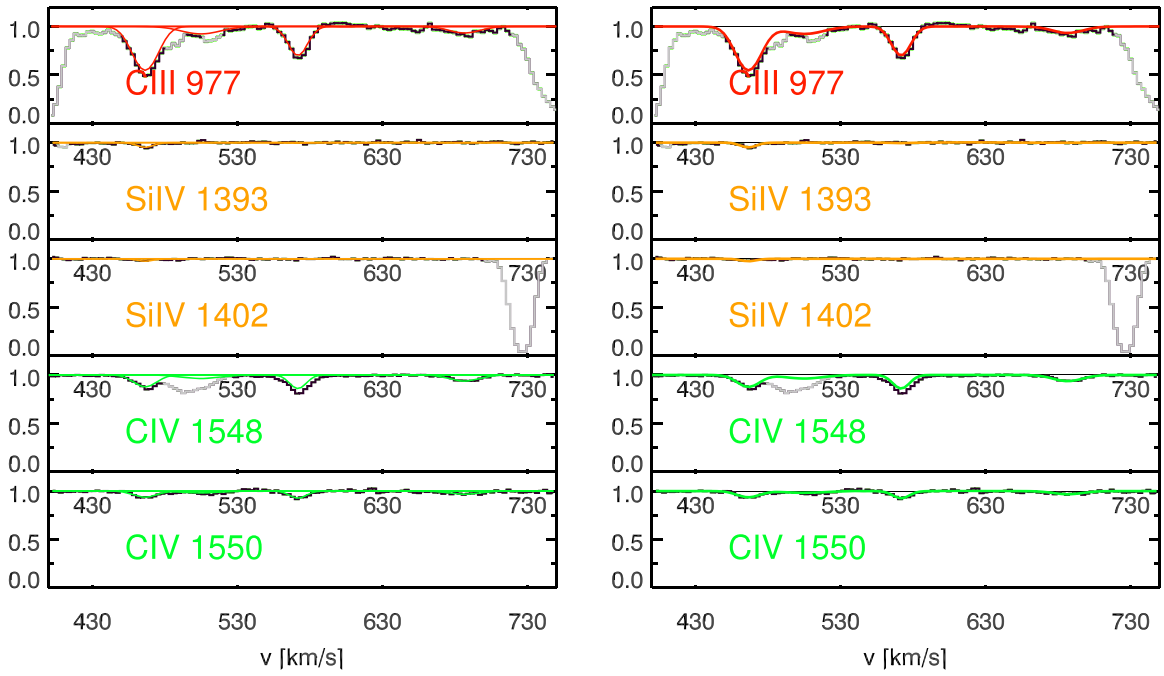

Figure 16. Same as Figure 15 but shown for Q0105-BX90b for the velocity range $400 < v < 750$ km s^{-1}.

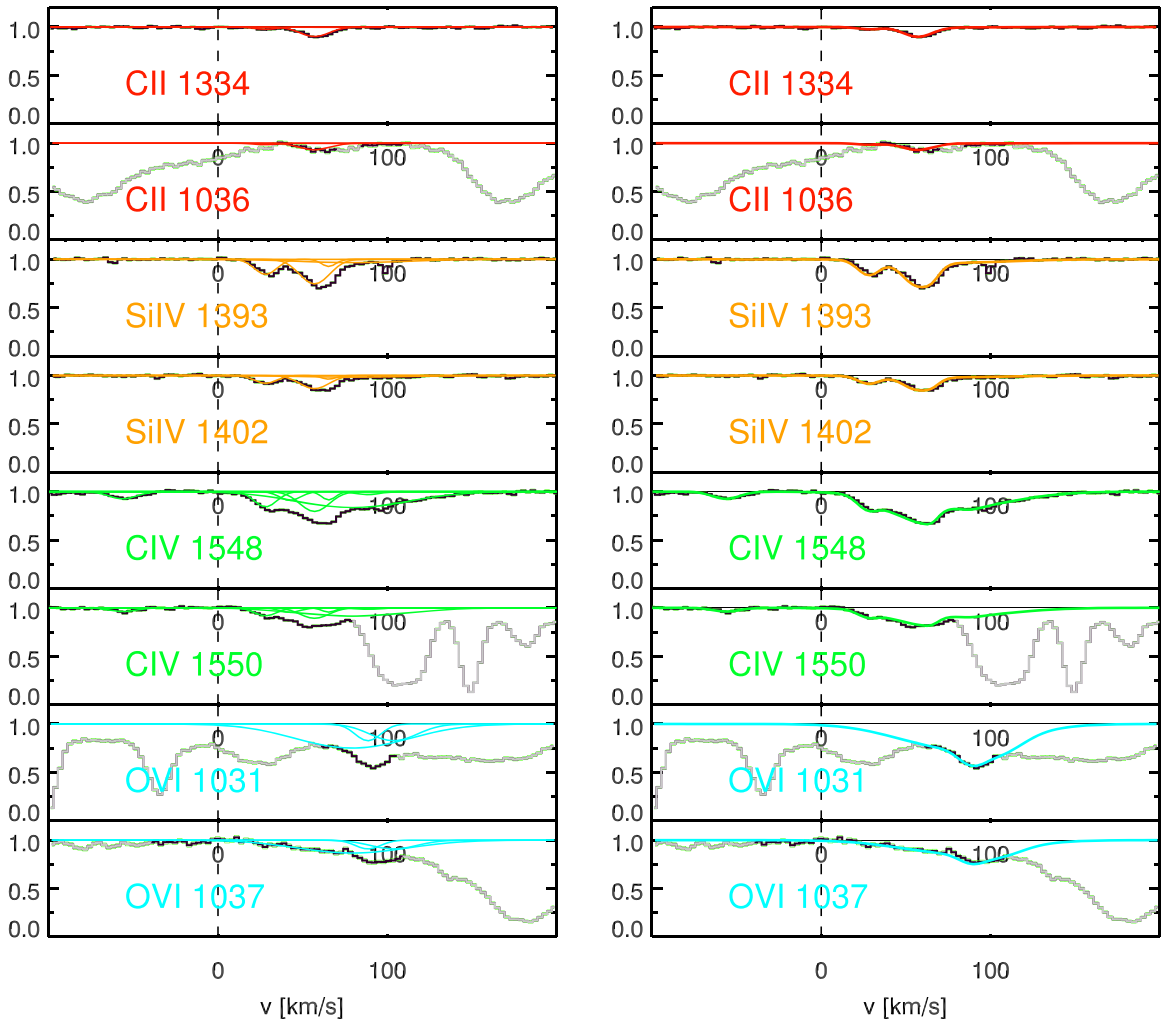

Figure 17. Same as Figure 15 but shown for Q1442-MD50a for the velocity range $-100 < v < 200$ km s^{-1}.

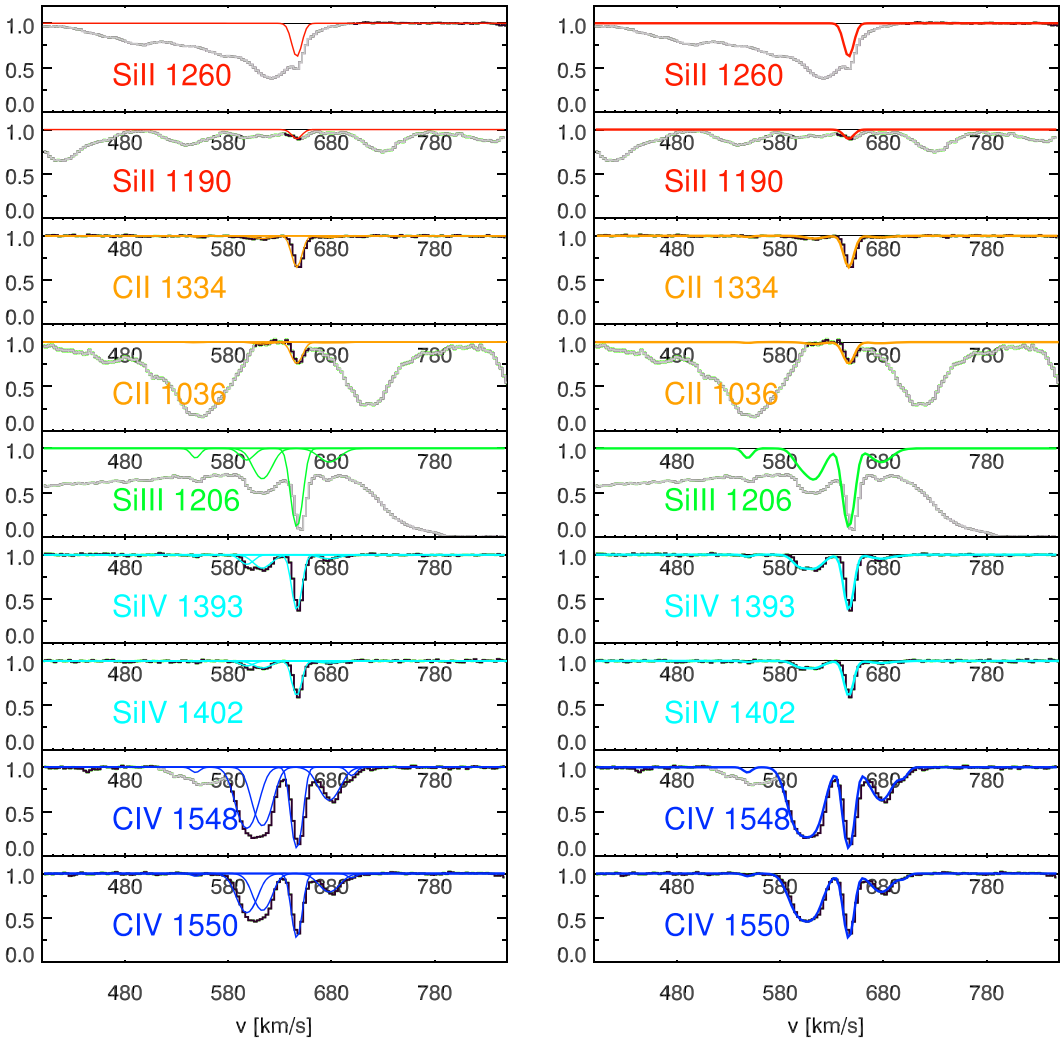

Figure 18. Same as Figure 15 but shown for Q1442-MD50a for the velocity range $400 < v < 850$ km s^{-1}.

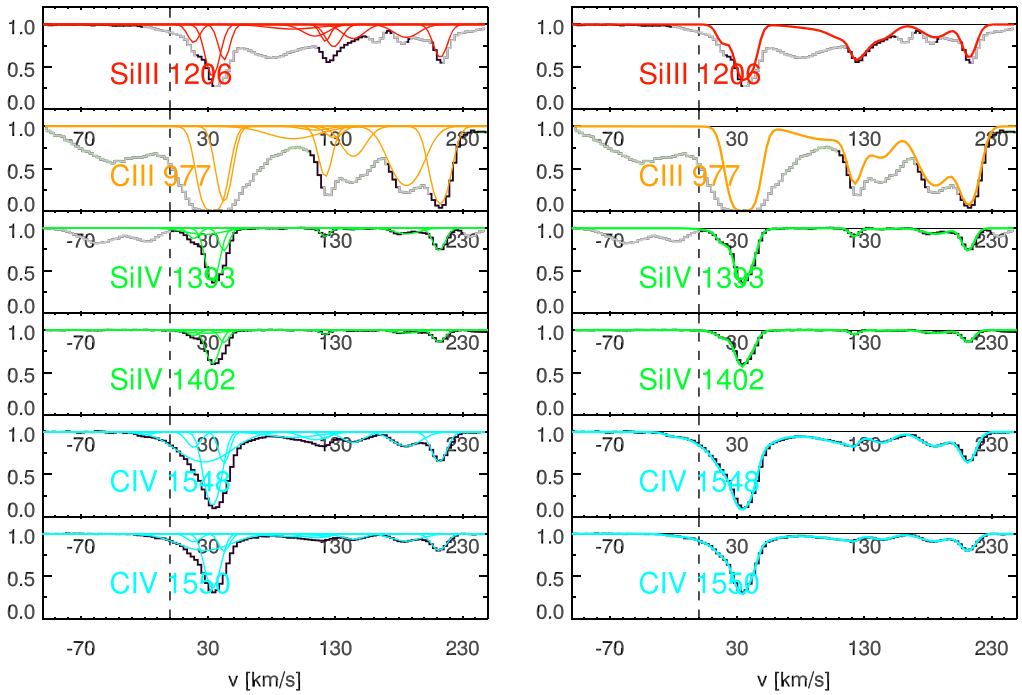

Figure 19. Same as Figure 15 but shown for Q1549-D15 for the velocity range $-100 < v < 250$ km s^{-1}.

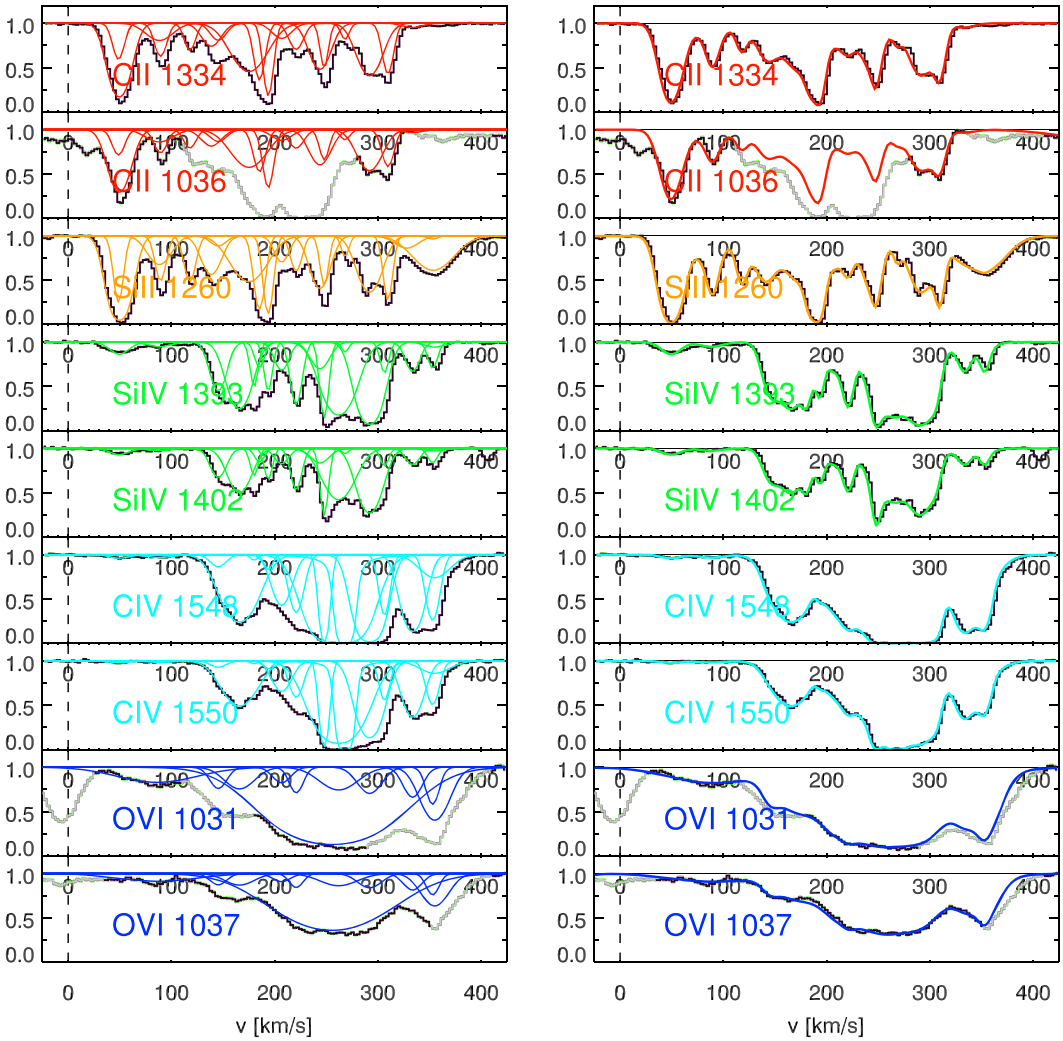

Figure 20. Same as Figure 15 but shown for Q1442-MD50b for the velocity range $-25 < v < 425$ km s^{-1}.

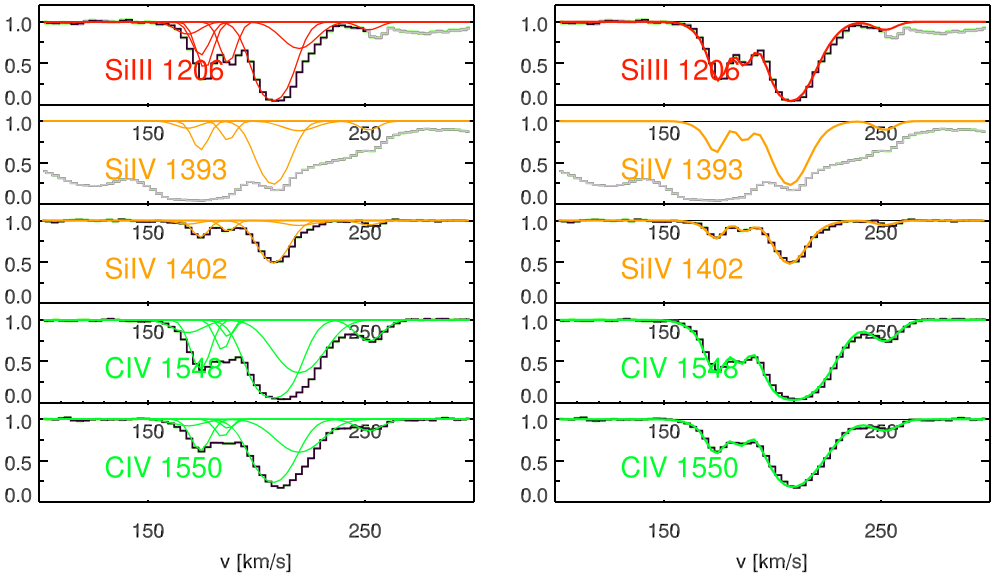

Figure 21. Same as Figure 15 but shown for Q2343-BX551 for the velocity range $100 < v < 300$ km s^{-1}.

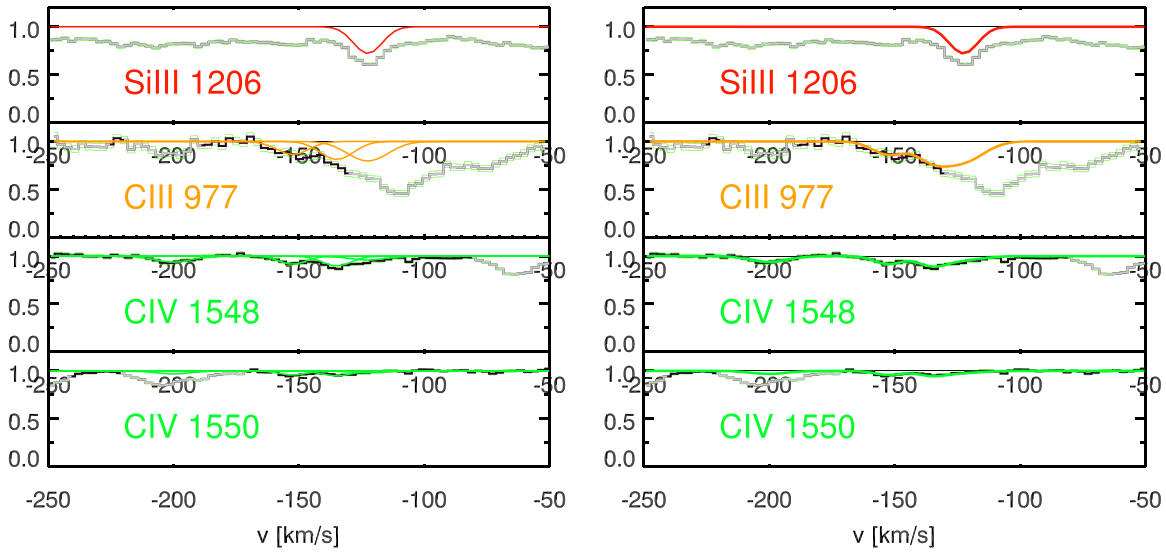

Figure 22. Same as Figure 15 but shown for Q0100-BX210 for the velocity range $-250 < v < -50$ km s^{-1}.

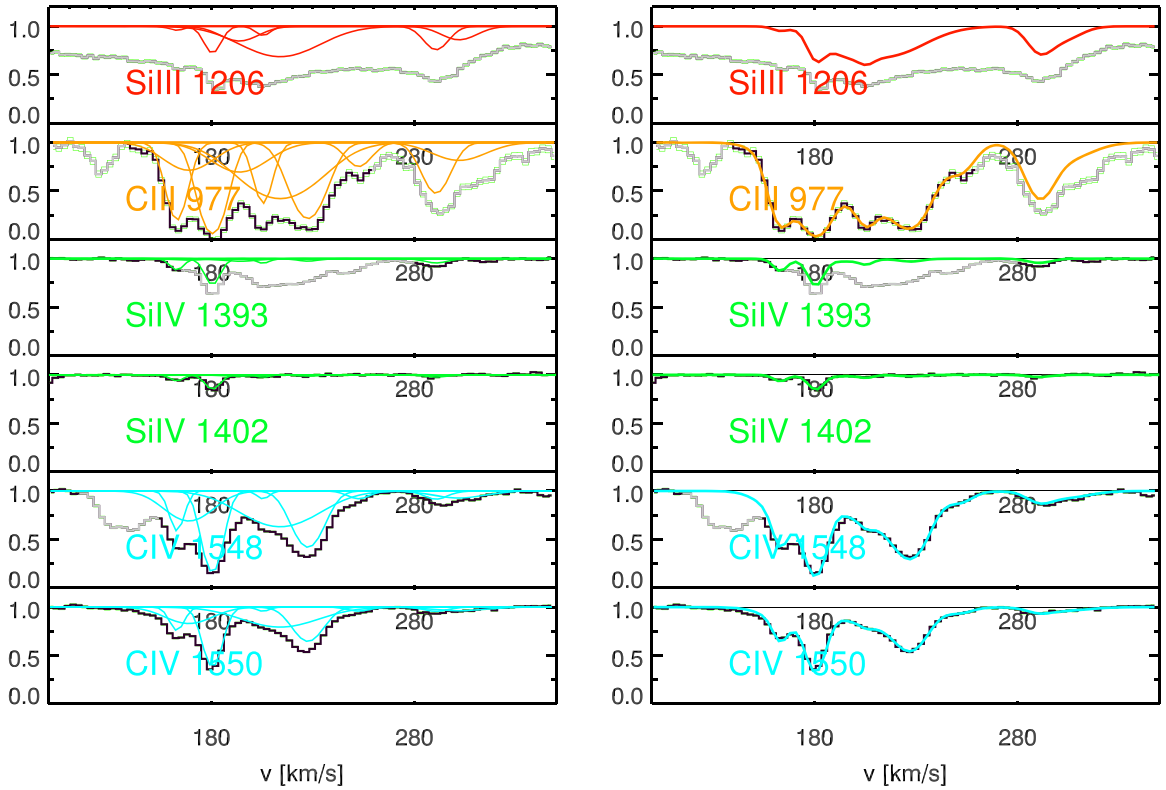

Figure 23. Same as Figure 15 but shown for Q0100-BX210 for the velocity range $100 < v < 350$ km s^{-1}.

ORCID iDs

Gwen C. Rudie https://orcid.org/0000-0002-8459-5413
Charles C. Steidel https://orcid.org/0000-0002-4834-7260
Ryan F. Trainor https://orcid.org/0000-0002-6967-7322
Allison L. Strom https://orcid.org/0000-0001-6369-1636
Cameron B. Hummels https://orcid.org/0000-0002-3817-8133
Naveen A. Reddy https://orcid.org/0000-0001-9687-4973
Alice E. Shapley https://orcid.org/0000-0003-3509-4855

References

Adelberger, K. L., Shapley, A. E., Steidel, C. C., et al. 2005, ApJ, 629, 636
Adelberger, K. L., Steidel, C. C., Shapley, A. E., et al. 2004, ApJ, 607, 226
Adelberger, K. L., Steidel, C. C., Shapley, A. E., & Pettini, M. 2003, ApJ, 584, 45
Anglés-Alcázar, D., Faucher-Giguère, C.-A., Kereš, D., et al. 2017, MNRAS, 470, 4698
Asplund, M., Grevesse, N., Sauval, A. J., & Scott, P. 2009, ARA&A, 47, 481
Behroozi, P. S., Wechsler, R. H., & Conroy, C. 2013, ApJ, 770, 57
Benson, A. J., & Bower, R. 2011, MNRAS, 410, 2653
Birnboim, Y., & Dekel, A. 2003, MNRAS, 345, 349

Booth, C. M., Agertz, O., Kravtsov, A. V., & Gnedin, N. Y. 2013, ApJL, 777, L16
Bordoloi, R., Tumlinson, J., Werk, J. K., et al. 2014, ApJ, 796, 136
Bordoloi, R., Wagner, A. Y., Heckman, T. M., & Norman, C. A. 2017, ApJ, 848, 122
Borthakur, S., Heckman, T., Strickland, D., Wild, V., & Schiminovich, D. 2013, ApJ, 768, 18
Borthakur, S., Heckman, T., Tumlinson, J., et al. 2016, ApJ, 833, 259
Brooks, A. M., Governato, F., Quinn, T., Brook, C. B., & Wadsley, J. 2009, ApJ, 694, 396
Bruzual, G., & Charlot, S. 2003, MNRAS, 344, 1000
Burchett, J. N., Tripp, T. M., Bordoloi, R., et al. 2016, ApJ, 832, 124
Butsky, I. S., & Quinn, T. R. 2018, ApJ, 868, 108
Chabrier, G. 2003, PASP, 115, 763
Chen, H., Wild, V., Tinker, J. L., et al. 2010, ApJL, 724, L176
Chen, H.-W., Gauthier, J.-R., Sharon, K., et al. 2014, MNRAS, 438, 1435
Chen, H.-W., & Mulchaey, J. S. 2009, ApJ, 701, 1219
Cooke, R., Pettini, M., Steidel, C. C., et al. 2010, MNRAS, 409, 679
Crighton, N. H. M., Bielby, R., Shanks, T., et al. 2011, MNRAS, 414, 28
Dai, X., Kochanek, C. S., Chartas, G., et al. 2010, ApJ, 709, 278
Dalgarno, A., & McCray, R. A. 1972, ARA&A, 10, 375
Dekker, H., D'Odorico, S., Kaufer, A., Delabre, B., & Kotzlowski, H. 2000, Proc. SPIE, 4008, 534
Duffy, A. R., Schaye, J., Kay, S. T., & Dalla Vecchia, C. 2008, MNRAS, 390, L64
Erb, D. K., Steidel, C. C., Shapley, A. E., et al. 2006, ApJ, 646, 107
Faerman, Y., Sternberg, A., & McKee, C. F. 2017, ApJ, 835, 52
Faucher-Giguère, C.-A., Kereš, D., & Ma, C.-P. 2011, MNRAS, 417, 2982
Fielding, D., Quataert, E., McCourt, M., & Thompson, T. A. 2017, MNRAS, 466, 3810
Ford, A. B., Davé, R., Oppenheimer, B. D., et al. 2014, MNRAS, 444, 1260
Fox, A. J., Ledoux, C., Petitjean, P., & Srianand, R. 2007a, A&A, 473, 791
Fox, A. J., Petitjean, P., Ledoux, C., & Srianand, R. 2007b, A&A, 465, 171
Girichidis, P., Naab, T., Hanasz, M., & Walch, S. 2018, MNRAS, 479, 3042
Gnat, O. 2017, ApJS, 228, 11
Gnat, O., & Sternberg, A. 2007, ApJS, 168, 213
Gronke, M., & Oh, S. P. 2018, MNRAS, 480, L111
Hafen, Z., Faucher-Giguere, C.-A., Angles-Alcazar, D., et al. 2019, MNRAS, 488, 1248
Heckman, T. M., Norman, C. A., Strickland, D. K., & Sembach, K. R. 2002, ApJ, 577, 691
Hennawi, J. F., Prochaska, J. X., Burles, S., et al. 2006, ApJ, 651, 61
Huang, Y.-H., Chen, H.-W., Johnson, S. D., & Weiner, B. J. 2016, MNRAS, 455, 1713
Hui, L., & Gnedin, N. Y. 1997, MNRAS, 292, 27
Hummels, C. B., Smith, B. D., Hopkins, P. F., et al. 2019, ApJ, 882, 156
Jiménez-Vicente, J., Mediavilla, E., Kochanek, C. S., et al. 2014, ApJ, 783, 47
Johnson, S. D., Chen, H.-W., & Mulchaey, J. S. 2015, MNRAS, 449, 3263
Johnson, S. D., Chen, H.-W., Mulchaey, J. S., Schaye, J., & Straka, L. A. 2017, ApJL, 850, L10
Kacprzak, G. G., Churchill, C. W., & Nielsen, N. M. 2012, ApJL, 760, L7
Kereš, D., Katz, N., Weinberg, D. H., & Davé, R. 2005, MNRAS, 363, 2
Kim, T.-S., Carswell, R. F., & Ranquist, D. 2016, MNRAS, 456, 3509
Liang, C. J., & Chen, H.-W. 2014, MNRAS, 445, 2061
Liang, C. J., Kravtsov, A. V., & Agertz, O. 2016, MNRAS, 458, 1164
Liang, C. J., & Remming, I. S. 2018, arXiv:1806.10688
Madau, P., Ferguson, H. C., Dickinson, M. E., et al. 1996, MNRAS, 283, 1388
Maller, A. H., & Bullock, J. S. 2004, MNRAS, 355, 694
McCourt, M., Oh, S. P., O'Leary, R., & Madigan, A.-M. 2018, MNRAS, 473, 5407
McCourt, M., Sharma, P., Quataert, E., & Parrish, I. J. 2012, MNRAS, 419, 3319
McLean, I. S., Steidel, C. C., Epps, H., et al. 2010, Proc. SPIE, 7735, 77351E
McLean, I. S., Steidel, C. C., Epps, H. W., et al. 2012, Proc. SPIE, 8446, 84460J
McQuinn, M., & Werk, J. K. 2018, ApJ, 852, 33
Morgan, C. W., Kochanek, C. S., Morgan, N. D., & Falco, E. E. 2010, ApJ, 712, 1129
Morrissey, P., Matuszewski, M., Martin, D. C., et al. 2018, ApJ, 864, 93
Mudd, D., Martini, P., Zu, Y., et al. 2018, ApJ, 862, 123
Muratov, A. L., Kereš, D., Faucher-Giguère, C.-A., et al. 2017, MNRAS, 468, 4170
Muzahid, S., Srianand, R., Bergeron, J., & Petitjean, P. 2012, MNRAS, 421, 446
Navarro, J. F., Frenk, C. S., & White, S. D. M. 1997, ApJ, 490, 493
Nielsen, N. M., Kacprzak, G. G., Pointon, S. K., Churchill, C. W., & Murphy, M. T. 2018, ApJ, 869, 153
Nomoto, K., Tominaga, N., Umeda, H., Kobayashi, C., & Maeda, K. 2006, NuPhA, 777, 424
Ocvirk, P., Pichon, C., & Teyssier, R. 2008, MNRAS, 390, 1326
Oke, J. B., Cohen, J. G., Carr, M., et al. 1995, PASP, 107, 375
Oppenheimer, B. D., Davé, R., Kereš, D., et al. 2010, MNRAS, 406, 2325
Oppenheimer, B. D., & Schaye, J. 2013, MNRAS, 434, 1043
Oppenheimer, B. D., Segers, M., Schaye, J., Richings, A. J., & Crain, R. A. 2018, MNRAS, 474, 4740
Peeples, M. S., Corlies, L., Tumlinson, J., et al. 2019, ApJ, 873, 129
Peeples, M. S., Werk, J. K., Tumlinson, J., et al. 2014, ApJ, 786, 54
Pettini, M., Shapley, A. E., Steidel, C. C., et al. 2001, ApJ, 554, 981
Qu, Z., & Bregman, J. N. 2018, ApJ, 856, 5
Rakic, O., Schaye, J., Steidel, C. C., et al. 2013, MNRAS, 433, 3103
Rakic, O., Schaye, J., Steidel, C. C., & Rudie, G. C. 2012, ApJ, 751, 94
Rauch, M., Sargent, W. L. W., & Barlow, T. A. 2001, ApJ, 554, 823
Rauch, M., Sargent, W. L. W., Womble, D. S., & Barlow, T. A. 1996, ApJL, 467, L5
Reddy, N., Dickinson, M., Elbaz, D., et al. 2012a, ApJ, 744, 154
Reddy, N. A., Pettini, M., Steidel, C. C., et al. 2012b, ApJ, 754, 25
Richards, G. T., Strauss, M. A., Fan, X., et al. 2006, AJ, 131, 2766
Rubin, K. H. R., Diamond-Stanic, A. M., Coil, A. L., Crighton, N. H. M., & Moustakas, J. 2018, ApJ, 853, 95
Rubin, K. H. R., Hennawi, J. F., Prochaska, J. X., et al. 2015, ApJ, 808, 38
Rudie, G. C., Steidel, C. C., & Pettini, M. 2012a, ApJL, 757, L30
Rudie, G. C., Steidel, C. C., Trainor, R. F., et al. 2012b, ApJ, 750, 67
Rupke, D. 2018, Galax, 6, 138
Salem, M., Bryan, G. L., & Corlies, L. 2016, MNRAS, 456, 582
Savage, B. D., Kim, T. S., Wakker, B. P., et al. 2014, ApJS, 212, 8
Scannapieco, E. 2017, ApJ, 837, 28
Schaye, J., Theuns, T., Leonard, A., & Efstathiou, G. 1999, MNRAS, 310, 57
Schneider, E. E., Robertson, B. E., & Thompson, T. A. 2018, ApJ, 862, 56
Shapiro, P. R., & Field, G. B. 1976, ApJ, 205, 762
Shapley, A. E., Steidel, C. C., Pettini, M., & Adelberger, K. L. 2003, ApJ, 588, 65
Shen, S., Madau, P., Guedes, J., et al. 2013, ApJ, 765, 89
Simcoe, R. A., Sargent, W. L. W., & Rauch, M. 2002, ApJ, 578, 737
Simcoe, R. A., Sargent, W. L. W., Rauch, M., & Becker, G. 2006, ApJ, 637, 648
Smette, A., Surdej, J., Shaver, P. A., et al. 1992, ApJ, 389, 39
Smith, B. D., Bryan, G. L., Glover, S. C. O., et al. 2017, MNRAS, 466, 2217
Steidel, C. C., Adelberger, K. L., Shapley, A. E., et al. 2003, ApJ, 592, 728
Steidel, C. C., Erb, D. K., Shapley, A. E., et al. 2010, ApJ, 717, 289
Steidel, C. C., Rudie, G. C., Strom, A. L., et al. 2014, ApJ, 795, 165
Steidel, C. C., Shapley, A. E., Pettini, M., et al. 2004, ApJ, 604, 534
Steidel, C. C., Strom, A. L., Pettini, M., et al. 2016, ApJ, 826, 159
Stern, J., Faucher-Giguère, C.-A., Hennawi, J. F., et al. 2018, ApJ, 865, 91
Stern, J., Hennawi, J. F., Prochaska, J. X., & Werk, J. K. 2016, ApJ, 830, 87
Stocke, J. T., Keeney, B. A., Danforth, C. W., et al. 2013, ApJ, 763, 148
Strom, A. L., Steidel, C. C., Rudie, G. C., et al. 2017, ApJ, 836, 164
Strom, A. L., Steidel, C. C., Rudie, G. C., Trainor, R. F., & Pettini, M. 2018, ApJ, 868, 117
Surdej, J., Magain, P., Swings, J.-P., et al. 1987, Natur, 329, 695
Suresh, J., Nelson, D., Genel, S., Rubin, K. H. R., & Hernquist, L. 2019, MNRAS, 483, 4040
Tacconi, L. J., Genzel, R., Neri, R., et al. 2010, Natur, 463, 781
Theios, R. L., Steidel, C. C., Strom, A. L., et al. 2019, ApJ, 871, 128
Thom, C., & Chen, H.-W. 2008, ApJS, 179, 37
Thom, C., Tumlinson, J., Werk, J. K., et al. 2012, ApJL, 758, L41
Thompson, T. A., Quataert, E., Zhang, D., & Weinberg, D. H. 2016, MNRAS, 455, 1830
Tilton, E. M., Danforth, C. W., Shull, J. M., & Ross, T. L. 2012, ApJ, 759, 112
Trainor, R. F., & Steidel, C. C. 2012, ApJ, 752, 39
Tripp, T. M., Meiring, J. D., Prochaska, J. X., et al. 2011, Sci, 334, 952
Tripp, T. M., Sembach, K. R., Bowen, D. V., et al. 2008, ApJS, 177, 39
Tumlinson, J., Thom, C., Werk, J. K., et al. 2011, Sci, 334, 948
Tumlinson, J., Thom, C., Werk, J. K., et al. 2013, ApJ, 777, 59
Turner, M. L., Schaye, J., Crain, R. A., et al. 2017, MNRAS, 471, 690
Turner, M. L., Schaye, J., Steidel, C. C., Rudie, G. C., & Strom, A. L. 2014, MNRAS, 445, 794
Turner, M. L., Schaye, J., Steidel, C. C., Rudie, G. C., & Strom, A. L. 2015, MNRAS, 450, 2067
van de Voort, F., Schaye, J., Booth, C. M., & Dalla Vecchia, C. 2011, MNRAS, 415, 2782

van de Voort, F., Schaye, J., Booth, C. M., Haas, M. R., & Dalla Vecchia, C. 2011, MNRAS, 414, 2458
van de Voort, F., Springel, V., Mandelker, N., van den Bosch, F. C., & Pakmor, R. 2019, MNRAS, 482, L85
Vincenzo, F., Matteucci, F., Belfiore, F., & Maiolino, R. 2016, MNRAS, 455, 4183
Vogt, S. S., Allen, S. L., Bigelow, B. C., et al. 1994, Proc. SPIE, 2198, 362
Voit, G. M. 2019, ApJ, 880, 139
Voit, G. M., Meece, G., Li, Y., et al. 2017, ApJ, 845, 80
Werk, J. K., Prochaska, J. X., Cantalupo, S., et al. 2016, ApJ, 833, 54
Werk, J. K., Prochaska, J. X., Thom, C., et al. 2013, ApJS, 204, 17
Werk, J. K., Prochaska, J. X., Tumlinson, J., et al. 2014, ApJ, 792, 8
Woosley, S. E., & Heger, A. 2007, PhR, 442, 269
Zahedy, F. S., Chen, H.-W., Johnson, S. D., et al. 2019, MNRAS, 484, 2257
Zahedy, F. S., Chen, H.-W., Rauch, M., Wilson, M. L., & Zabludoff, A. 2016, MNRAS, 458, 2423
Zhu, G., Ménard, B., Bizyaev, D., et al. 2014, MNRAS, 439, 3139